EISCAT SPACE DEBRIS MEASUREMENTS 2006

J Markkanen
`jussi.markkanen@eiscat.sgo.fi`

DRAFT REPORT
of ongoing activity

August 1, 2006

1. Introduction

This evolving report summarizes EISCAT space debris (SD) measurements done in 2006, as of August 1, 2006. The work is a continuation of the development and measuring activities performed in 2000–2005 under three ESA contracts [1], [2], [3].[1] The debris measurements in EISCAT are conducted "biggy-backed" with our normal ionospheric measurements. In the spring 2006, EISCAT conducted a one month long measurement campaign, from March 06 to April 06, both with the UHF system in Tromsø and with the ESR system. In parallel to these measurements, we used the space debris receivers in Tromsø and on Svalbard to measure space debris. In Tromsø between March 13 and April 6, we measured 387 hours with the 930 MHz UHF system and and got, after the analysis, 6817 events. On Svalbard we measured 138 hours between March 17 and March 23, and got 5242 events. From 12 UT, July 8th to 12 UT, July 9th, we run a 24 hour debris measurement at ESR, as EISCAT's contribution to the international, IAD-coordinated, debris measurement campaign, using the 32 m ESR antenna. The measurement was the first time we fiddled an EISCAT standard measurement in a way to make the measurement more optimal for debris work , in this case, by increasing the pulse repetition period to 20 ms, to get an uninterrupted coverage over the whole LEO altitude interval, from 400 km to (over) 2000 km.

The debris measurements have been mainly my responsibility, but with essential and much appreciated help from staff at the Tromsø site (Arild) and Svalbard site (Anja, Halvard, Martin). I would also like to acknowledge the enthusiastic support of the director of EISCAT, prof. A van Eyken, for this work.

2. Tau2 cp1 campaign at Tromsø from March 13 to April 6

I drove from Sodankylä to Tromsø in the night between March 12 and March 13. There were no particular problems setting up the mothballed SD receiving system, and start the debris measurement at about 09 UT. The EISCAT experiment was the TAU2 experiment. The TAU2 transmission scheme is shown in Fig. 17 on p. 28. The Tromsø UHF antenna was parked to the magnetic field aligned direction, azimuth 185.1°and elevation 77.5°. Throughout the run, transmission peak power was about 1.2 MW. Even though the power varied somewhat as shown in Fig. 5 on p. 16, in debris analysis the constant value 1.2 MW has been used. The value 110 K was used for the system temperature.

A schematic drawing of the SD measuring hardware arrangement at the Tromsø site is shown in Fig. 2. The achieved range coverage and the applied detection threshold in TAU2 are indicated in Fig. 6. As shown in Fig. 3 and Fig. 4, the used detection threshold 5, in terms of the square root of ENR which is the ratio of the coherently integrated signal energy E_{sig} to the noise power spectral density kT_{sys}, $\text{ENR} = E_{\text{sig}}/kT_{\text{sys}}$, corresponds to a false alarm time of about 3 hours, and gives a minimum detectable target radar cross section (RCS) of 21 mm^2, and a minimum detectable effective diameter of 2.6 cm, at

---

[1] The final reports of the contracts are online at `http://www.eiscat.com/SpaceDebris/`, as are the actual measurement results of the July 2006 beam park measurement.

1000 km range.

Figures 7–13 plot in various ways the basic target parameters of the 6817 events collected during the TAU2 campaign.

3. Steffe cp1 campaign at ESR from March 17 to March 23

After having started up a debris measurement in Tromsø, I went up to Svalbard on Tuesday, March 14. The next day, March 15, was used in setting up the debris receiver hardware (Fig. 15 and Fig. 16), and convincing myself that the problem of not being able to properly restart the measurement under software (DROS) control, that had plagued the previous campaign on Svalbard, was still an unsurmountable problem. The only solution for the time being seems to be to try to record as long data streams as possible, and restart the recording manually, via a reboot of the data collection computer if necessary. This is a very bad solution though, as it entails a considerable operator load in running the experiment, and even more seriously, a lot of extra manual effort later on in organizing the final data to orderly, daily directories.

March 16 was spent in implementing the (for debris purposes) new STEFFE experiment in the data processing software. This first of all required some experimenting with suitable sampling rates. I ended up using 46 MHz primary sampling rate and total decimation 92, so the final sampling interval in the saved data is 2 μs. The 46 MHz primary sampling implies that the frequency $46/4 = 11.500$ MHz will be mapped to the zero-frequency in the demodulation and decimation process. This ensures that the shorter transmission of the two-pulse, two-frequency STEFFE transmission, Fig. 17, which has second IF frequency at 11.550 MHz, maps sufficiently near to DC so that no correction due to signal attenuation in the decimation filtering needs to be applied to it.

Another task was to select the part of the STEFFE transmission that could be best used for debris observations. Two two frequencies in STEFFE are separated by 400 MHz, so they cannot be squeezed to a 500 MHz band without bad attenuation of at least one of the channels. They could be handled together with 1000 MHz sampling. That was tried, and is possible. But a more serious problem related to the attainable range coverage nevertheless favors the utilization of only the shorter pulse in debris analysis. The strategy that I have used in most cases elsewhere, to use the *whole* (possibly multi-frequency) transmission sequence as a rigid pattern that is shifted in range and matched against the reception samples in the match function method (as in the upmost diagram of Fig. 18), would waste too much of the range coverage. This is because the debris data processing does not yet allow using a changing part of the transmission in the matching process, so the available ranges are determined in the spirit of Fig. 18.[2] I experimented using the whole of the shorter pulse and the whole of the longer pulse separately in the analysis of data taken with 1000 MHz final sampling (so that both channels were clearly visible; this analysis and the raw data of the events have been saved, but I do not handle them further in this report). Even when used alone, the longer pulse still leads to intolerably large range gaps as seen in the bottom panel of Fig. 19, so for this campaign

---

[2] Fixing this nuisance would be one of the first “exercises for the student”, would I have one.

at least, I ended up using only the shorter pulse, even though that means totally wasting three quarters of the available transmission duty cycle. With 9735 μs IPP, the effective transmission RF-duty cycle with the short pulse is 5.1% (which incidentally still is not too bad among the world's high-power radars). The summary in Fig. 23 shows, we were able to observe quite a decent amount of events even with this duty cycle. The mean event rate of about 38 events per hour during a 138 hour, essentially uninterrupted measurement is about twice as high as we have been able to get at the Tromsø UHF system.

4. A 24-hour IADC beam park campaign at ESR July 8th–9th

As EISCAT's contribution to the international IADC debris campaign we conducted a 24-hour measurement at the EISCAT Svalbard radar (ESR) from 12 UT July 8th to 12 UT July 9th. For the measurement, we used the smaller of the two ESR antennas, the 32 m antenna, pointed to azimuth 90°(East) and elevation 75° (Fig. 31). The antenna has gain 42.5 dBi and half-power beam width 1.09°. A measured gain pattern for the ESR 32 m antenna is not available; as a substitute, an idealized antenna pattern is shown in Fig. 32, together with the actual measured pattern of EISCAT's 930 MHz 32 m antenna of Tromsø, scaled to 500 MHz wavelength. The geographic location of the ESR site is latitude 78.15313°N, longitude 16.02875°E, altitude 445 m. EISCAT pointing geometry program uses geocentric cartesian coordinates $x = 1262.647$ km, $y = 362.744$ km, $z = 6220.902$ km and a spheroid with axis 6378.135 km and 6356.75 km.

We used a modified version of the standard EISCAT ESR experiment STEFFE, resulting an experiment we call STEFFELEO. The standard STEFFE has two frequency channels, one transmitting a 480 us binary phase coded pulse intended for the lower ionosphere, the other transmitting a 1680 us binary phase coded pulse for higher altitudes. The two pulses are separated by 1520 us, and the arrangement repeats every 9375 us. Two modifications were made to the STEFFE transmission. First, the repetition period was increased to 20 000 μs to obtain uninterrupted altitude coverage over the whole LEO, and second, the transmission frequencies were adjusted slightly, so that the two frequencies were more suitably located for the space debris receiver sampling system. In STEFFELEO, the shorter pulse is transmitted at 500.4 MHz and the longer one at 500.1 MHz. After downconversion, these frequencies appear at 10.85 MHz and 11.15 MHz at the radar's second IF, where they are sampled by the EISCAT debris receiver using primary sampling rate of 44 MHz. After demodulation by Hilbert-transform and sampling rate reduction to final 1 MHz complex sampling rate, the two frequency channels are centered at +150 kHz and -150 kHz in the base-band, as shown in Fig. **??**.

For the analysis presented here, we have only made use of the longer of the two pulses, so the effective transmission duty cycle was 8.5%. We processed the recorded data both using coherent pulse-to-pulse integration within our match function method (FMF) and by non-coherent pulse-to-pulse integration (NCI). These methods are described in **??**. Target detection was done using 15-pulse (0.3 s) integration. For the coherent integration, detection threshold was set to $\widehat{\mathrm{ENR}} = 24$, corresponding to false alarm time of 10 hours, and for the non-coherent integration, the threshold was set to $\widehat{\mathrm{ENR}} = 39$, corresponding to false alarm time of 24 hours (Fig. 34). Due to ionospheric clutter, for ranges below 750 km in NCI, and below 600 km in FMF, range-dependent threshold was used, as shown in Fig. 39. It must be noted that for noise background subtraction, the same range-independent value was used throughout in analysis (ENR= 1 in FMI, and ENR= 15 in NCI). This is not correct for the region of range-dependent threshold, but affects only relatively small number of events.

For these integration arrangements, ideally the coherent integration is expected to be 2.0 dB more sensitive in terms of the smallest detectable ENR (Fig. 35), but, after final analysis, the two methods gave essentially identical sensitivity, especially for ranges grater than 750 km where constant threshold could be used, see Fig. 42. With the NCI, the final object count was 1629 objects, with FMF, 1659 objects. These counts include objects up to our maximum range of 2400 km, but only 16 (NCI) and 12 (FMF) objects with range larger than 2053 km (which corresponds to the high end of the LEO region at 2000 km altitude) were detected.

Figure 42 shows the estimated ENR for all objects, and objects with ranges beyond 750 km, in both integration schemes. Figure 44 gives the minimum compatible cross section $\mathrm{RCS}_{\mathrm{min}}$, computed from Eq. (15). Figure 45 shows the the effective diameter. The effective diameter is computed from the radar cross section using a simplified cross section model which joins the Rayleigh and optical regions, ignoring the resonance region, as shown in Fig. 37. At the ESR wavelength, the simplified model overestimates the size of objects in the about 10–20 cm effective diameter class, resulting in an artificially large step at about 10 cm size in histograms such as Fig. 45.

Figure 41 shows the range-rate measurement.

ASCII-format listings of the EISCAT beam-park measurement results are publicly available via our web page at `http://www.eiscat.com/SpaceDebris/`.

References

[1] J. Markkanen, M. Lehtinen, A. Huuskonen and A. Väänänen, Measurements of Small-Size Debris with Backscatter of Radio Waves, (Final Report, ESOC Contract No. 13945/99/D/CD, 2002).

[2] J. Markkanen and M. Postila, Real-time Small-Size Debris Detection with EISCAT Radar Facilities, (Final Report, ESOC Contract No. 16646/02/D/HK(CS), 2005).

[3] J. Markkanen and M. Postila, Small-Size Space Debris Data Collection with EISCAT Radar Facilities, (Final Report, ESOC Contract No. 18575/04/D/HK(SC), 2006).

A. Summary of our coherent and non-coherent integration methods.

A.1. Coherent integration in the match function method

The complex-valued signal $z(t)$ consists of target echo $s(t)$ and noise,

$$z(t) = s(t) + \gamma(t)\,. \tag{1}$$

During a time interval $[0, T_\mathrm{c}]$, the integration time—we typically use T_c= 0.2–0.3 s– $s(t)$ is modeled as a delayed-in-time, Doppler-shifted replica of the transmission $x(t)$,

$$s(t) = b_0 x(t - 2R_0/c)\mathrm{e}^{-i2\pi \frac{v_0}{\lambda/2} t}\,, \tag{2}$$

where R_0 is target range, v_0 is target radial velocity in the radar frame of reference, and λ is the radar wavelength. In EISCAT space debris measurements, in addition to $z(t)$, also $x(t)$ is measured, so that Eq. (2) provides a three-parameter set of model functions to be matched against the measured $z(t)$.

We assume that the echo stays coherent, that is, the model Eq. (2) holds, during the integration time, a few tens of interpulse periods (IPPs). Then it is possible to use coherent integration in target detection. The match function method of coherent pulse-to-pulse integration is based on computing the quantity that is often called the radar ambiguity function in the literature, but which we choose to term the match function. The match function is a function of the range gate $R_j = j\tau_\mathrm{s}c/2$, where τ_s is the sampling interval, and the Doppler-velocity v, which is the radial component of the velocity vector (positive away from the radar). The MF is computed from the sampled signal vector $\mathbf{z}$ and the transmission-sample vector $\mathbf{x}$ as

$$\mathrm{MF}(v, R_j) = \frac{|\sum_n z_n \overline{x}_{n-j} \mathrm{e}^{i2\pi \frac{v}{\lambda/2} n\tau_\mathrm{s}}|}{\|\mathbf{x}\|}\,, \tag{3}$$

where

$$\|\mathbf{x}\| = (\sum_n |x_n|^2)^{1/2}\,. \tag{4}$$

It follows from Eq. (3) that at the velocity points

$$v_k = \frac{k}{N_\mathrm{DFT}} \frac{\lambda}{2} \frac{1}{\tau_\mathrm{s}} \tag{5}$$

the MF can be computed using discrete Fourier-transform. For a fixed range, the function $v \mapsto \mathrm{MF}(v, R_j)$ is essentially the spectrum of the cross-correlation vector $\mathbf{w}^{(j)} : w_n = z_n \overline{x}_{n-j}$; we refer to it as the MF velocity slice through the range R_j. Figure 1 summarizes the match function computation. There we also show an extra step that we normally take to speed up the computations: basically, we just drop out the “unnecessary” zeros that occur in the DFT input vector due to the pulsed transmission. We call the resulting algorithm the fast match function algorithm, FMF. The gain of speed is large, typically

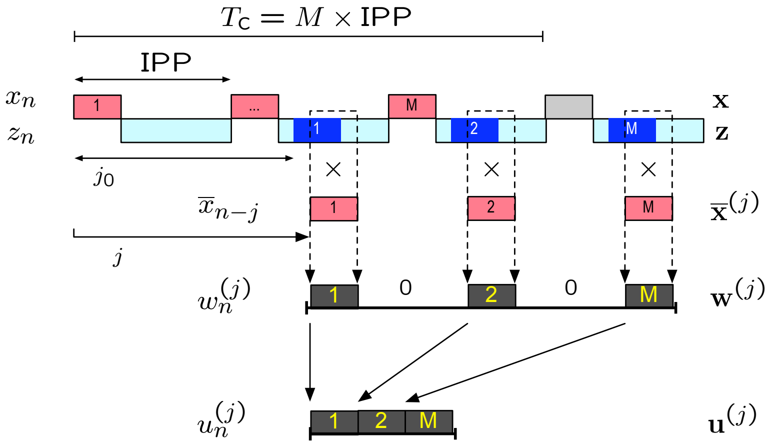

Figure 1: Coherent integration of M pulses in the MF- and FMF-algorithms. The raw data are the complex transmission samples x_n and the noisy reception samples $z_n = s_n + \gamma_n$. The diagram also indicates an echo of a point-target at range R_{j_0}. To evaluate the match function $\mathrm{MF}(R, v)$ at range R_j and velocity v_k, the first step is to point-wise multiply the reception vector $\mathbf{z}$ with the time-shifted, complex-conjugated transmission vector $\overline{\mathbf{x}}^{(j)}$, to produce the vector $\mathbf{w}^{(j)}$. The magnitude of the discrete Fourier-transform of $\mathbf{w}^{(j)}$, normalized by $\|\mathbf{x}\|$, gives a velocity slice of the match function: $\mathrm{MF}(j, k) = |\mathrm{DFT}\{\mathbf{w}^{(j)}\}(k)|/\|\mathbf{x}\|$. Computation of the fast match function FMF has an extra step before the Fourier-transform: the M non-zero blocks of $\mathbf{w}^{(j)}$ are concatenated, to the much shorter vector $\mathbf{u}^{(j)}$. The normalized magnitude of $\mathrm{DFT}\{\mathbf{u}^{(\mathrm{j})}\}$ is a velocity slice in the FMF.

more than two orders of magnitude, so we almost always use FMF in the practical computations. The gain in speed comes with a price, since the detection sensitivity in the FMF-scheme is slightly reduced compared to the MF.

If there is no noise, the position of the MF maximum gives the target range R_0 and radial velocity v_0,

$$\arg\max_{v,R} \mathrm{MF}(v,R) = (v_0, R_0)\,,$$

and the value of the maximum is proportional to the square root of the total signal energy E_s ($\propto \|\mathbf{s}\|^2$). Even with noise, we use the position of the MF maximum as an estimate of the target range and Doppler-velocity,

$$(\widehat{v}, \widehat{R}) = \arg\max_{v,R} \mathrm{MF}(v,R)\,, \tag{6}$$

and expect the MF maximum value still to be a reasonable estimate for $\|\mathbf{s}\|$. With noise, we need also consider background subtraction. We assume that the maximum of the noisy MF takes place near the position (v_0, R_0), and form the expectation value of MF^2. Assuming that the noise samples γ_n are zero mean, independent, complex gaussians with variance σ^2, one gets

$$\mathrm{E}\left(\max \mathrm{MF}^2\right) \approx \|s\|^2 + \sigma^2\,. \tag{7}$$

This shows that to get an unbiased estimate of $\|s\|^2$, we have to subtract the noise power from the MF^2 maximum value,

$$\widehat{\|\mathbf{s}\|^2} = \max \mathrm{MF}^2 - \sigma^2\,. \tag{8}$$

With coherent integration, the minimum detectable signal will have $\max \mathrm{MF}^2 \gtrsim 25\,\sigma^2$ in our case, so the subtraction has only a minor effect to the estimate. With non-coherent integration, the background subtraction is essential.

The norm $\|\mathbf{s}\|$ of the received signal is related to the actual energy $E_{s'} = \int |s'(t)|^2 dt$ of the incoming signal $s'(t)$ in front of the receiver by

$$\tau_\mathrm{s} \|\mathbf{s}\|^2 = g E_{s'}\,, \tag{9}$$

where τ_s is the sampling interval, provided that the signal is of sufficiently narrow bandwidth so that there is not much aliasing, and that the receiver power gain g can be taken to be constant across the signal bandwidth. We divide the receiver gain such that $g = g_\mathrm{A} \cdot G$, where g_A is the gain of the relatively wide-band analog receiver and G is the precisely calculable gain of the digitally implemented space debris receiver. We take g_A to be a constant over the whole bandwidth of the SD receiver. We get rid of the unknown gain g_A by noting that the noise power after the receiver, σ^2, estimated as the variance of the reception samples z_n in the absence of signal, is

$$\sigma^2 = k_\mathrm{B} T_\mathrm{sys} g_\mathrm{A} B_\mathrm{eq}\,, \tag{10}$$

where B_eq is the noise-equivalent bandwidth of the SD receiver, and $k_\mathrm{B} T_\mathrm{sys}$ is the power spectral density of the wide-band noise in front of the receiver, which we take to be a known radar parameter. The impulse response of the SD receiver is constructed to be of constant value $1/\tau_\mathrm{s}$ and duration equal to τ_s. For such a system, $B_\mathrm{eq} = 1/\tau_\mathrm{s}$ so that, from Eq. (8)–(10), we get

$$\frac{\widehat{E_{s'}}}{k_\mathrm{B} T_\mathrm{sys}} = \frac{1}{G}\left(\frac{\max \mathrm{MF}^2}{\sigma^2} - 1\right) . \tag{11}$$

In practice, we take G to be unity, and drop the prime from $E_{s'}$. We call the dimensionless ratio of the total signal energy divided by the noise power spectral density (= noise power per unit bandwith) the "energy-to-noise ratio" ENR,

$$\mathrm{ENR} \equiv \frac{E_s}{k_\mathrm{B} T_\mathrm{sys}} . \tag{12}$$

Thus, we estimate the energy-to-noise ratio from the MF maximum value as

$$\widehat{\mathrm{ENR}} = \frac{\max \mathrm{MF}^2}{\sigma^2} - 1 . \tag{13}$$

Equation (13) has two related uses. First, it gives the target detection criterion for the threshold detection: with threshold Θ,

$$\text{detection} \leftrightarrow \sqrt{\widehat{\mathrm{ENR}} + 1} \; > \; \Theta . \tag{14}$$

We try to set the threshold Θ to be so high that there are only "very few" false alarms. Experience has shown that, with the coherent integration times 0.2–0.3 s that we normally use with the EISCAT standard experiments, the value $\Theta = 5$ is a suitable starting point. In the Final Report we give some theoretical justification for that choice, showing that it corresponds to a false alarm time of a few hours. The standard threshold might need to be increased sometimes, typically during strong auroral events, due to clutter. Then we normally increase Θ perhaps up to 7, but only in those ranges where the ionospheric clutter actually is a problem. On the other hand, we try to keep the threshold setting intact during a single measurement campaign. Normally the ionospheric clutter is a problem only at altitudes up to about 500 km, and their range aliases.

The second use of Eq. (11) is to estimate the target "size". We treat the system temperature as a known radar parameter, and use the measured MF maximum to get estimate of the ENR. We use these to find a lower limit, $\mathrm{RCS}_\mathrm{min}$, for the target's radar cross section (RCS). From the standard radar equation it follows

$$\mathrm{RCS} = \frac{(4\pi)^3 \, k_\mathrm{B} T_\mathrm{sys} \cdot R^4 \cdot \mathrm{ENR}}{G(\phi)^2 \cdot \lambda^2 \cdot P_x \cdot \mathcal{D} T_c} . \tag{15}$$

Here R is target range, λ is radar wavelength, P_x transmission peak power, $\mathcal{D}$ transmission duty cycle so that $\mathcal{D} T_c$ is the actual length of transmission during the integration T_c. The factor $G(\phi)$ is the antenna power gain in the direction of the target within the radar beam, an angle ϕ offset from the known direction of the antenna optical axes. In the EISCAT system, it is normally not possible to find the offset angle. As a way of cataloguing the observed signal strength, we therefore normally quote $\mathrm{RCS}_\mathrm{min}$, which we get from Eq. (15) by setting $\phi = 0$.

A.2. Non-coherent integration in the match function method

We always process a single pulse coherently. Even though really really a misnomer, considering the fact that we actually, in the single pulse, add coherently about 1000 samples, and then non-coherently only a few tens pulses, we use the expression “non-coherent integration”, when we add squares of the single-pulse match functions, in the similar way as we would add power from several pulses. Using non-coherent integration places less demands for the coherence time of the signal. On the other hand, if the signal is coherent, phase information is unnecessarily lost in the squaring. More precisely, we implement the non-coherent integration via maximization, over the range and velocity parameters, of the non-coherent match function $\mathrm{MF}_{\mathrm{nc}}$, which we define by [3]

$$\mathrm{MF}_{\mathrm{nc}}(R, v) \equiv \sqrt{\sum_{m=0}^{M-1} [\mathrm{MF}(m; R, v)]^2} \,. \tag{16}$$

The maximum value of ${\mathrm{MF}_{\mathrm{nc}}}^2/\sigma^2$ is roughly equal to the sum of the background level (unity) and the mean of the energy-to-noise-ratios computed separately for each pulse, multiplied by the number of pulses:

$$\frac{\max_{v,R}(\mathrm{MF}_{\mathrm{nc}})^2}{\sigma^2} \approx M \times (1 + \frac{\mathrm{ENR}}{M}) = \mathrm{ENR} + M \,. \tag{17}$$

---

[3] In our report [3], and elsewhere, we have included a division by M inside the square root. Leaving it out causes both coherent and non-coheren integrations to give numerically roughly equal MF values, which is more convenient.

B. FIGURES

List of Figures

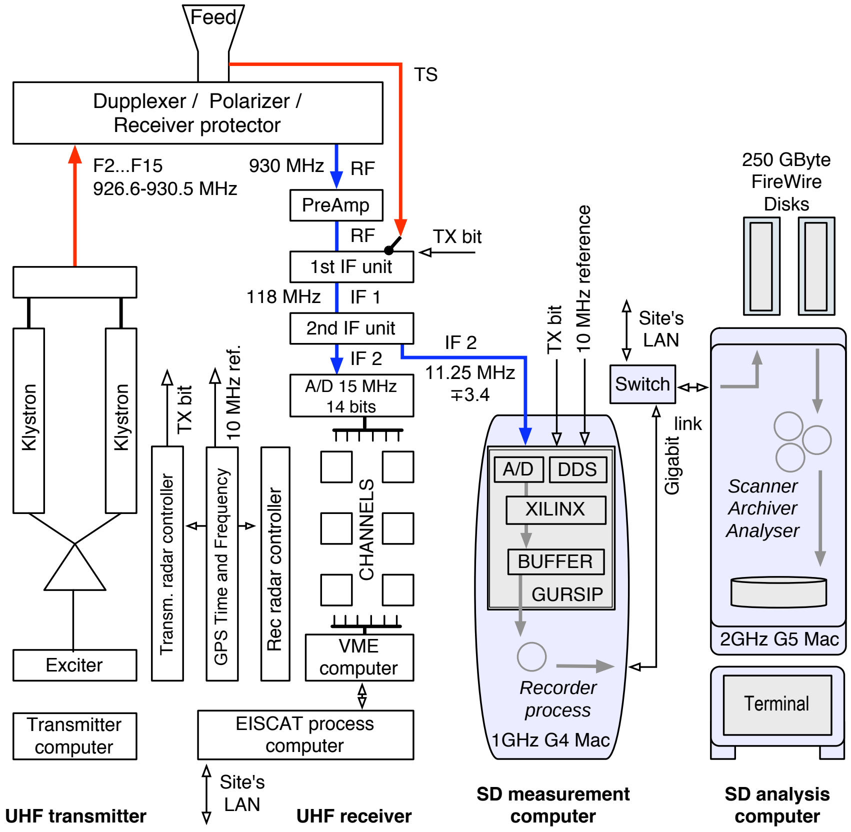

Figure 2: The Tromsø UHF radar and the space debris receiver. The SD receiver consists of a measurement computer and an analysis computer. The measurement computer hosts a custom signal processing board (GURSIP). The primary analog input to the SD receiver is the EISCAT second intermediate frequency (IF 2) band. The input contains, time-multiplexed, both the standard received signal and the transmission sample signal (TS). On the processing board, there is an analog-to-digital converter (A/D) taking 40–46 megasamples per second; a direct-digital-synthesizer chip (DDS), which provides clock signals on the board, phase-locked to the host radar's 10 MHz frequency reference signal; two Xilinks signal processing chips (XILINX) to perform signal demodulation and sampling rate reduction; and a memory buffer for temporary storage of the samples. The recorder program running on the measurement computer moves the samples over a gigibit network link to an external FireWire disk, mounted on the analysis computer. Target detection is done by the scanner program running on the analysis computer, using the match function method. It is also possible to move all the computations into the measurement computer, when the processing needs are modest. After failure of the G5, this was done in the March-April TAU2 campaign. The console terminal was not used either, all monitoring and control access was done over network using VNC. For the last 10 days of the run, this was done from Sodankylä over the internet.

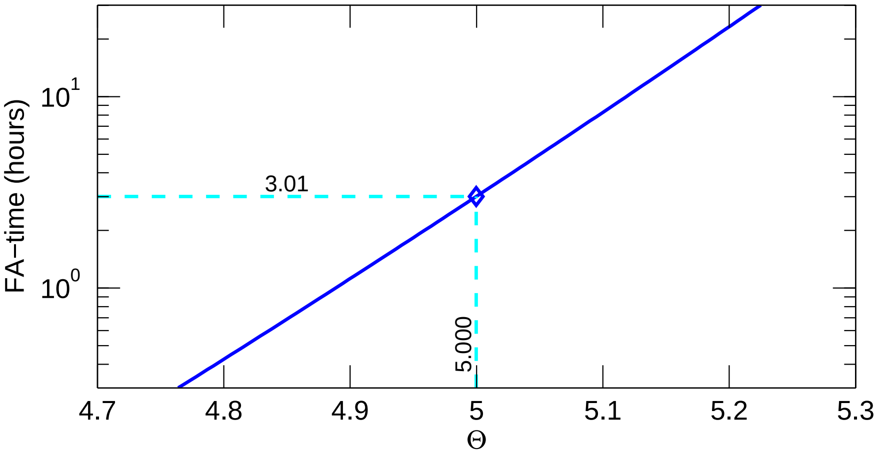

Figure 3: False alarm time v detection threshold in TAU2 in coherent integration. The plot is based on Eq. (2.27) in [3], with 1000 range gates and maximum monitored velocity 5 $\mathrm{km\,s^{-1}}$. The actual number of range gates searched in detection was 1013, but these would not all be statistically independent, and the false alarm time, 3 hours for the detection threshold 5.0, is probably a slight underestimate. The threshold Θ is in terms of $\max \mathrm{MF}/\sigma = \sqrt{\mathrm{ENR}+1}$.

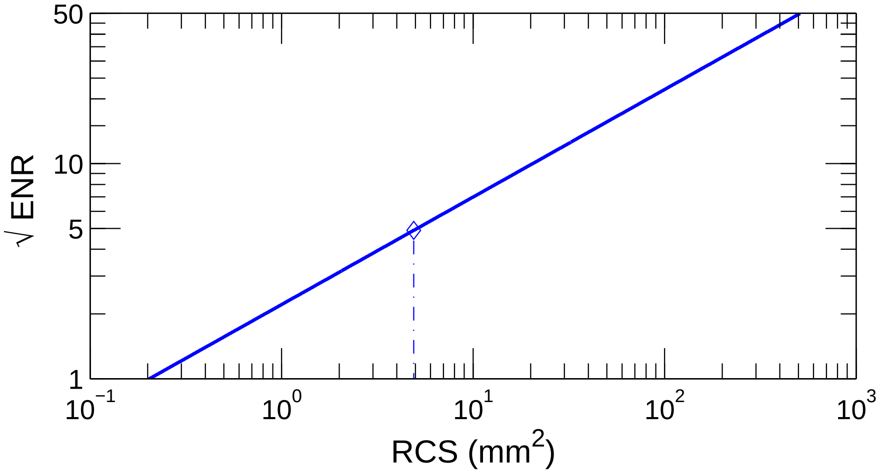

Figure 4: Expected energy-to-noise ratio as function of RCS in TAU2. The UHF, 930 MHz, 32 m antenna with gain 48.1 dBi, range 1000 km, system temperature 110 K and 0.2 s coherent integration are assumed. RCS 20.7 mm^2 corresponds to our standard detection threshold ENR = 24. The corresponding effective diameter is 2.62 cm.

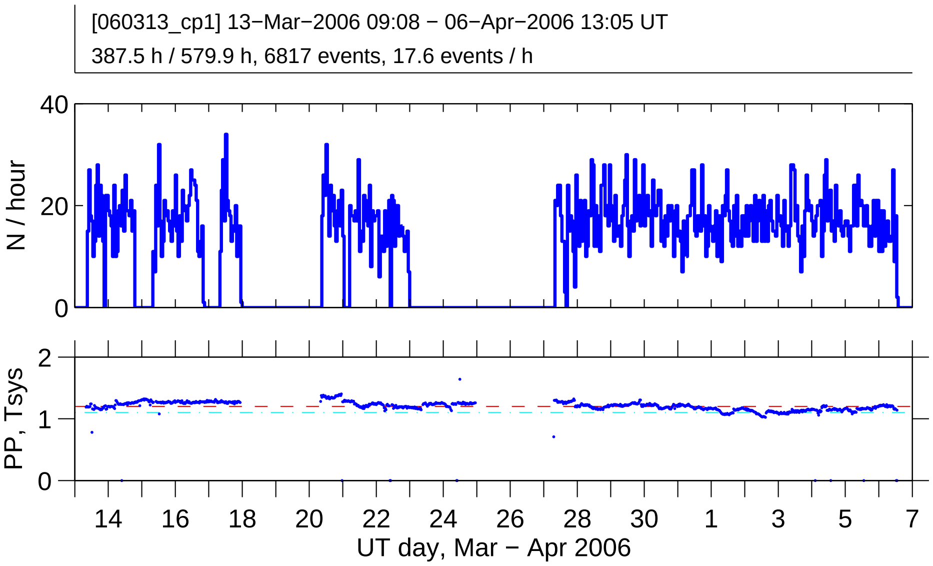

Figure 5: Summary of TAU2 CP1 campaign at Tromsø, March–April 2006. The header panel gives the start and stop times of the debris measurement, the total length of "valid" data collection (found by adding up all half-hour intervals between the campaign start and end times during which the final analysis found at least one event), the number of analysed events, and the mean number of analysed events per the valid data collection time. The middle panel gives the hourly number of debris events. There are several long gaps in the debris data collection. First of all, during March, EISCAT only measured during the normal working days Monday-Friday in Tromsø [sic]. In addition, on debris data collection stopped twice due to computer failure (the system complained about overheating and went to sleep). These events were not immediately notices. After the second failure soon after midnight March 23, it took until I get back to from Svalbard to Tromso on March 24 to reconfigure the system to use only a single computer. Then I drove back to Sodankylä, and run the rest of the campaign, ten days, without any interruption remotely. The blue line in the bottom panel gives the transmission peak power in MW. The red dashed line at 1.2 MW indicates the value used in debris analysis.

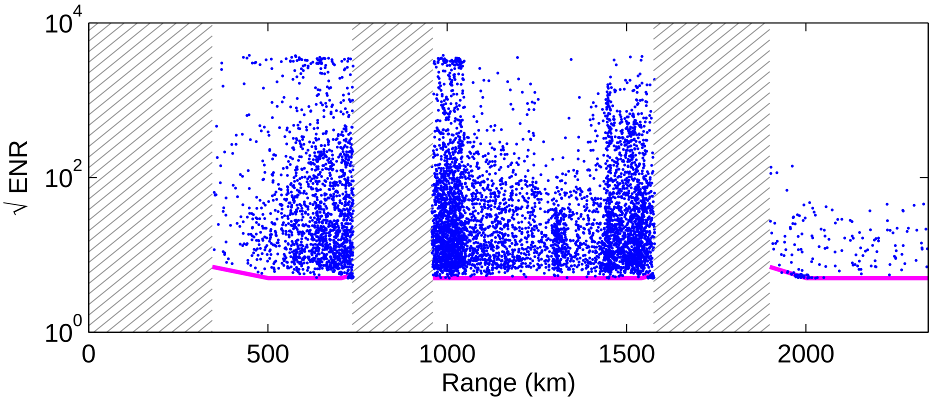

Figure 6: TAU2 at UHF, March–April 2006, signal energy versus range, all events. The y-axis is the maximum value of the match function divided by noise standard deviation. Apart from a not-subtracted noise background of unity, this is equal to the square root of the signal energy-to-noise ratio ENR $= E_\mathrm{s}/kT_\mathrm{sys}$; more precisely, y-axis could be labeled with $\sqrt{\mathrm{ENR}+1}$. The detection threshold is a line with vertexes at (x, y)-points (375,7), (501,5), (705,5), (735,5.5); (960,5), (1542,5), (1575,5.5); (1899,7), (2001,5), (2379.5) and (2409,5.5) (the last vertex it not visible in this figure). The downward ramps are to counteract clutter due to the topside ionosphere. The upwards ramps are to counteract calibration noise injection. For thermal noise, and fully efficient coherent integration, the base threshold level 5 corresponds to false alarm time of about three hours in this experiment. The constancy over range of the maximum observed ENR indicates that the strongest signals have been clipped by the receiver.

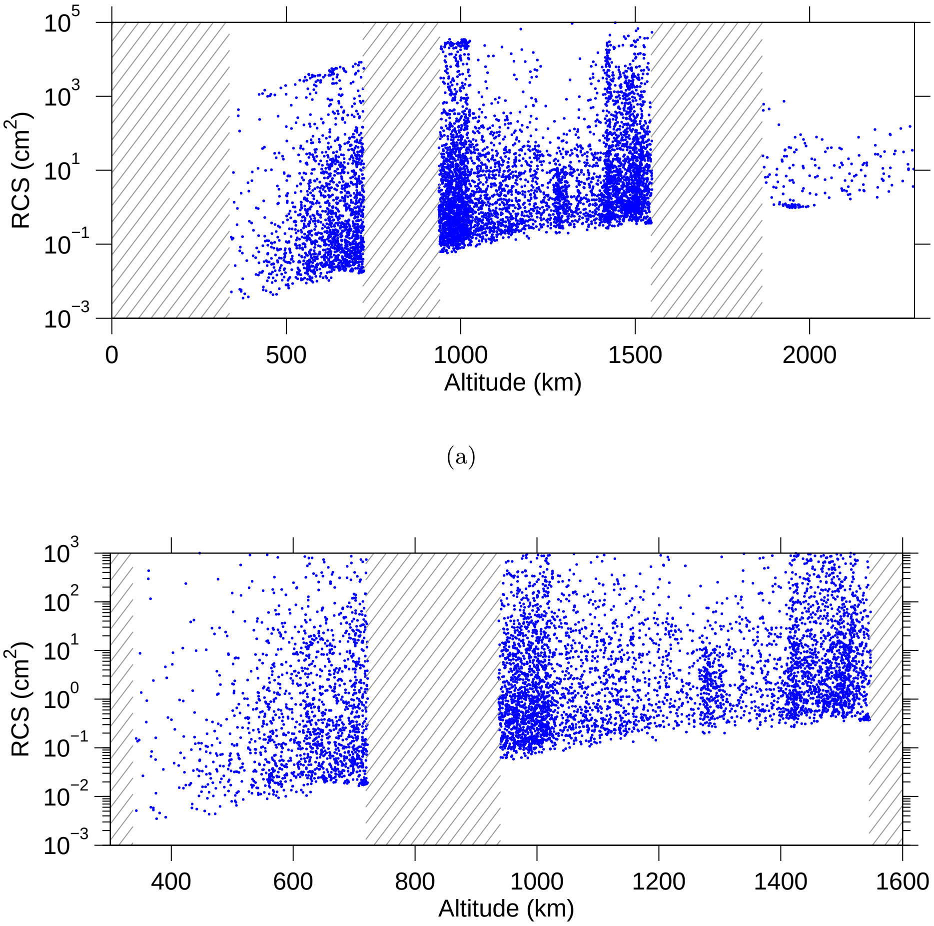

(a)

(b)

Figure 7: TAU2 at UHF, March–April 2006, cross section versus altitude.

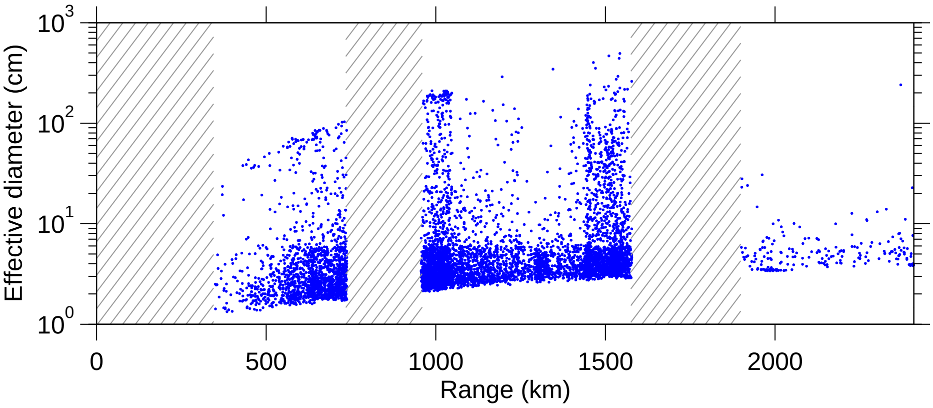

(a) All events.

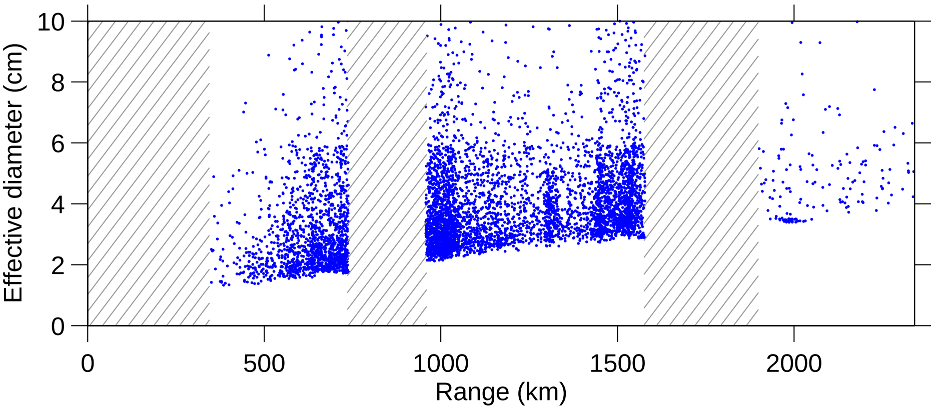

(b) Detail.

Figure 8: TAU2 at UHF, March–April 2006, effective diameter versus range. The step at about 6 cm size is an artifact due to the simplified conversion from radar cross section to effective diameter, which ignores the resonance region.

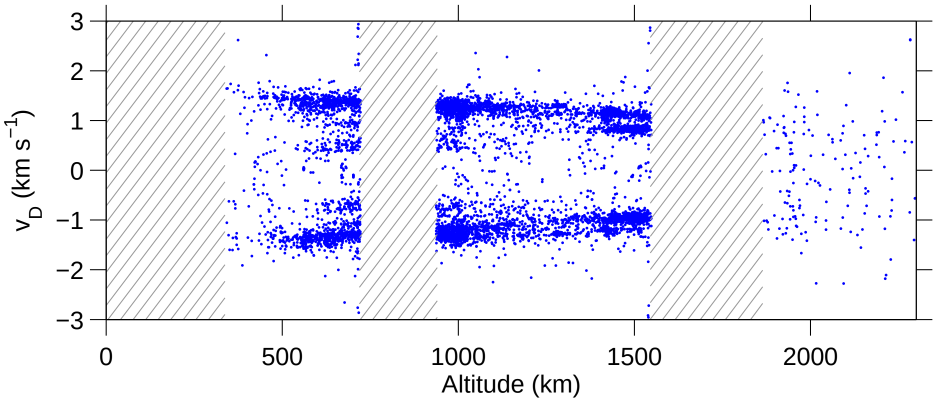

(a) All events.

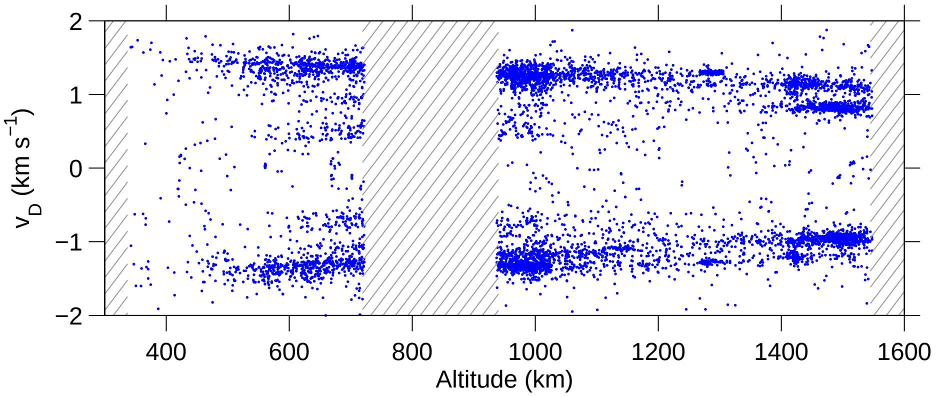

(b) Detail.

Figure 9: TAU2 at UHF, March–April 2006, Radial velocity v altitude.

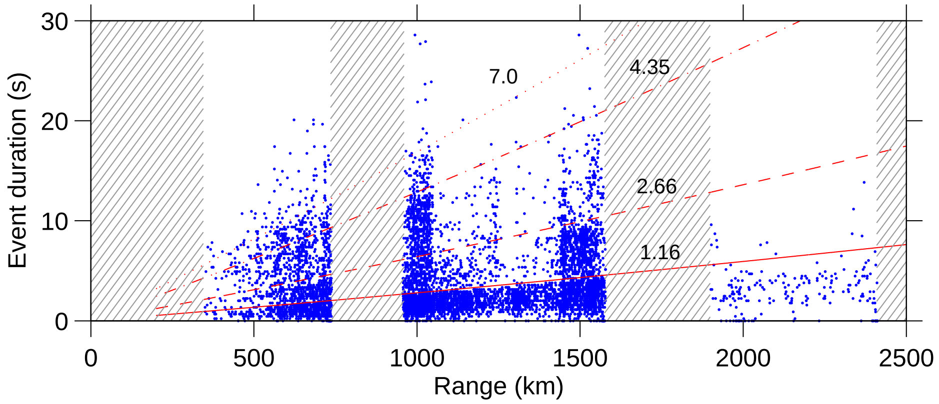

(a) All data.

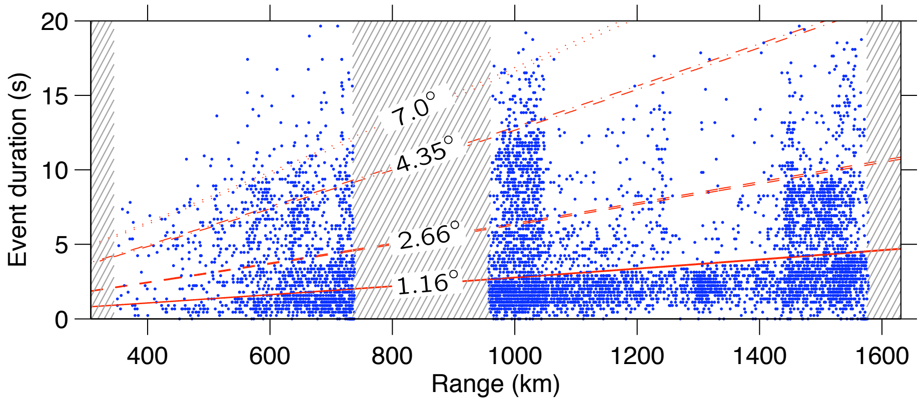

(b) Detail.

Figure 10: TAU2 at UHF, March–April 2006, event duration versus range. The oblique lines indicate event duration corresponding the indicated field-of-view for circular orbits. There appears to be discontinuities in the event distributions near these boundaries. The discontinuities may be associated with the discontinuous change of detection sensitivity when a new side lobe is taken into use. For instance, the FOV of 1.16° is entirely within the main beam lobe. The one-way gain at offset 0.58° is about -14dB down from the maximum gain of the main lobe, but equals to the maximum gain of the first side lobe. That means that, for a given range, up to a certain size, targets will be visible only in the main lobe. (For instance, at 1000 km range with 0.2 s coherent integration in TAU2, targets with effective diameter of less than 10.7 cm will only be visible in the main lobe.) But targets that are any bigger, are visible also in the much wider beam, and therefore, the number of detections will tend to increase discontinuously; therefore, there will be a marked deficiency in the number of events durations that are only a little longer than the duration corresponding to the 1.16° FOV.

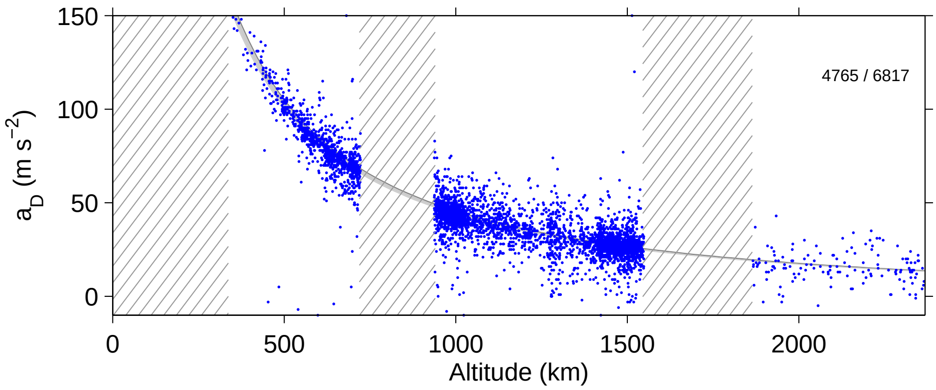

(a)

Figure 11: TAU2 at UHF, March–April 2006, radial acceleration versus altitude. This figure must be understood as a "sanity check" only. With the simple-minded application of the FMF method that was used in the analysis, determination of the radial acceleration in individual events is noisy to the extend of being almost meaningless.

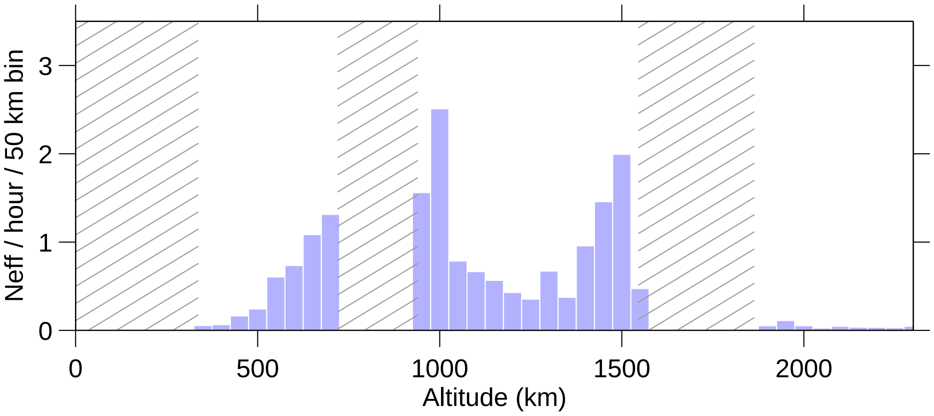

(a) All events.

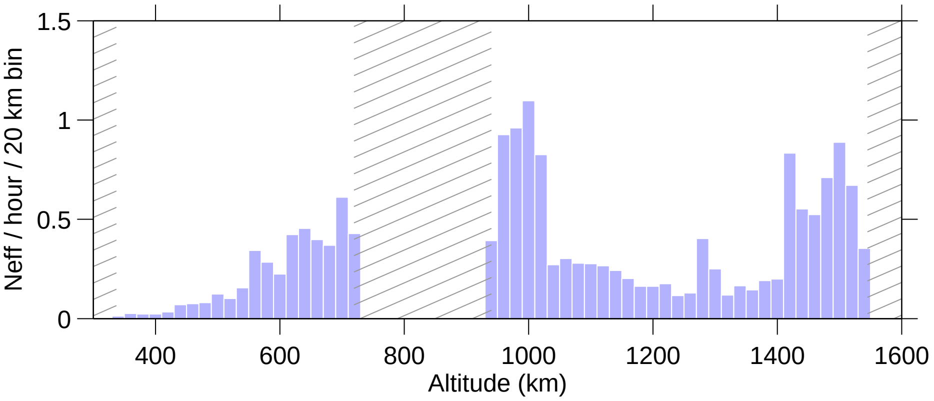

(b) Detail.

Figure 12: TAU2 at UHF, March–April 2006, event rate as function of altitude.

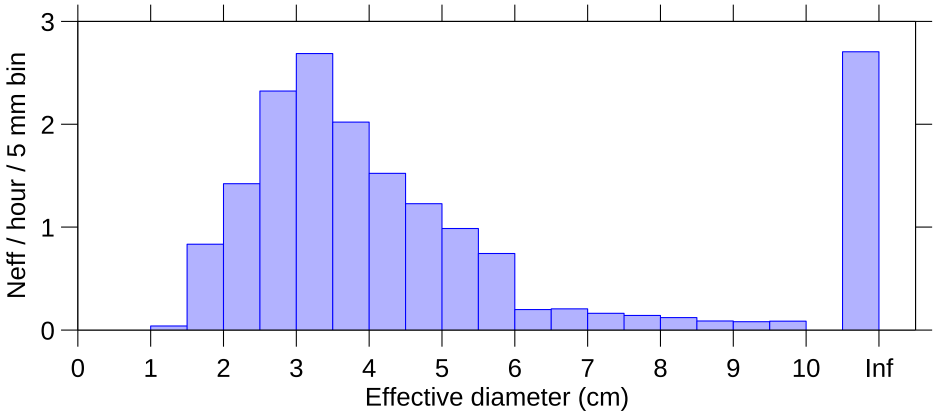

(a)

Figure 13: TAU2 at UHF, March–April 2006, event rate as function of effective diameter.

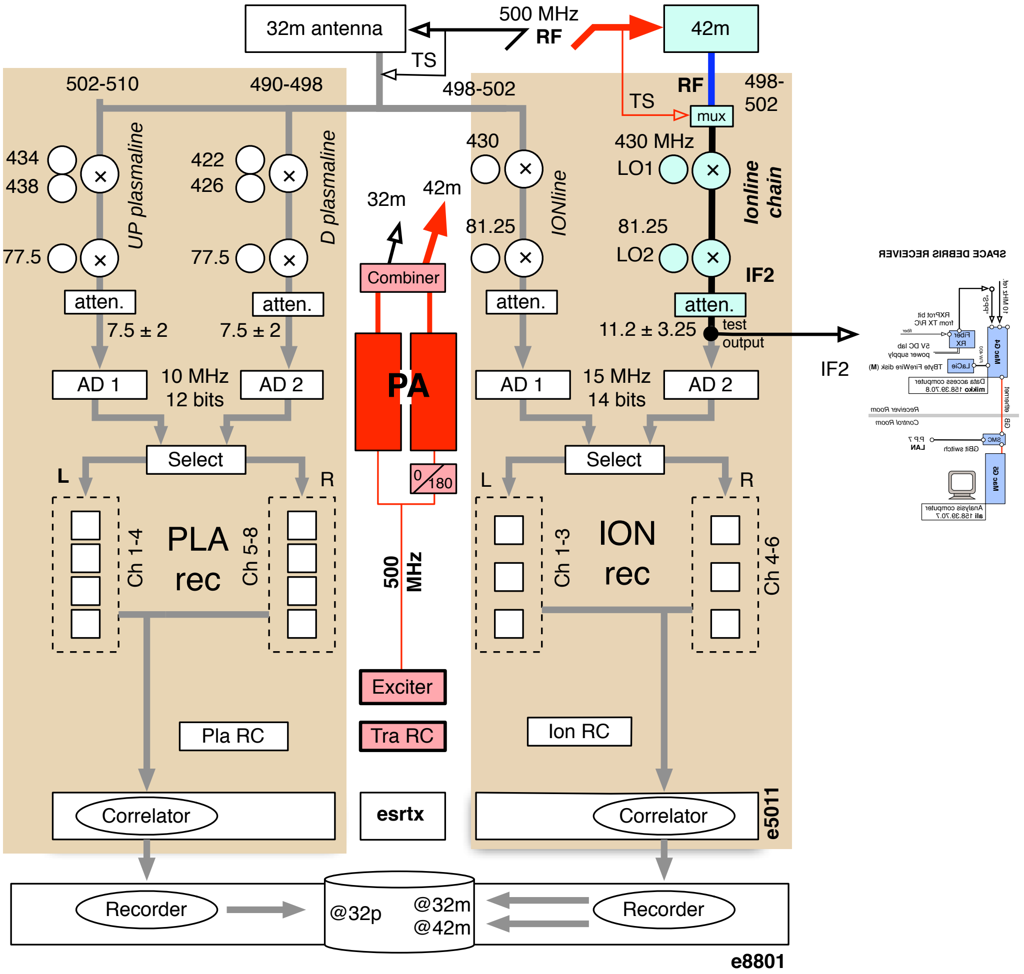

Figure 14: The ESR radar and the space debris receiver. The principal data flow during the STEFFE CP1 measurement, from the space debris receiver point of view. The radar has a single transmitter, two antennas, and four complete receiver chains. In the STEFFE CP1 scheme, the transmitter output is switched permanently to the 42 m antenna, while both antennas are used for reception. The space debris receiver, hooked to the second analog IF (IF2) of the receiver chain coming down from the 42 m antenna, records continuously, receiving either the standard echo, or the transmission sample signal (TS). In addition to the analog IF2, the SD-receiver records the control bit (not shown) that switches the system between transmit and receive states. See Fig. 15 for an enlarged drawing of SD receiver part of the diagram.

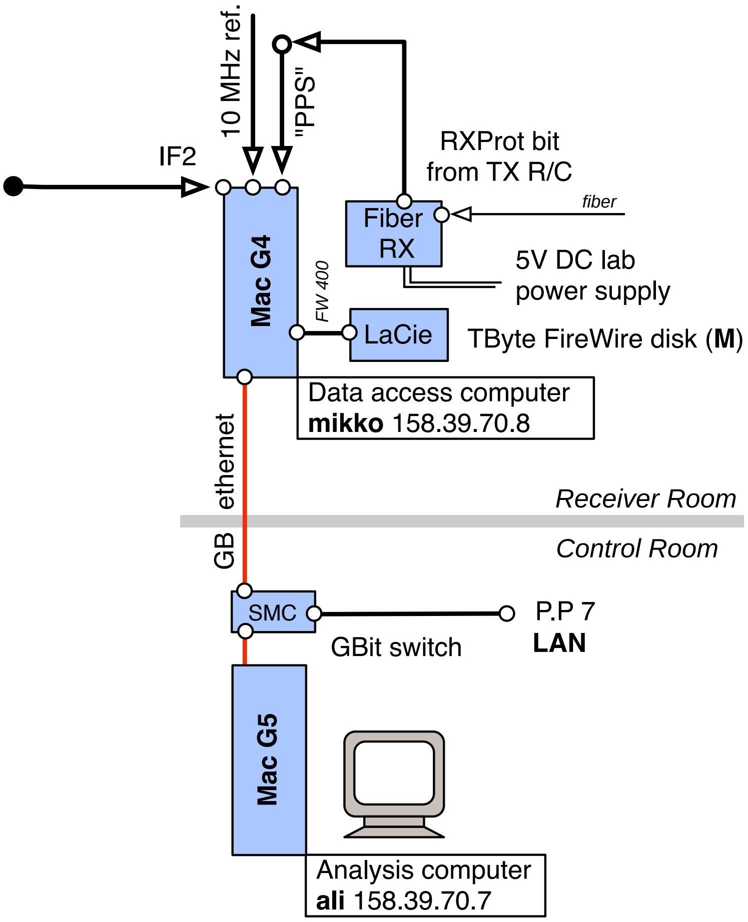

Figure 15: The space debris receiver at the ESR radar.

Figure 16: The ESR antennas and the SD receiver. Panel (a) shows the 42 m diameter, magnetic field aligned antenna (1), the fully steerable 32 m antenna (2), staff engineer Langteigen (3) and site leader Boholm (4), the all four approximately field-aligned in 20 $\mathrm{m\,s^{-1}}$ wind and -20 C temperature, on the slope of the Breinosa mounting at about 400 m altude, at latitude 78.153°N, on March 22. Panel (b) shows the Macintosh G5 analysis computer (5), the gigabit switch (6) and the console screen (7). Panel (c) shows the Macintosh G4 measurement computer, with the external connections: gigabit ethernet to the analysis computer (8), IF2 signal from the radar's analog receiver (9), phase-locked 10 MHz frequency reference signal from the radar's frequency distribution system (10), and the receiver protector bit from the transmitter radar controller (11).

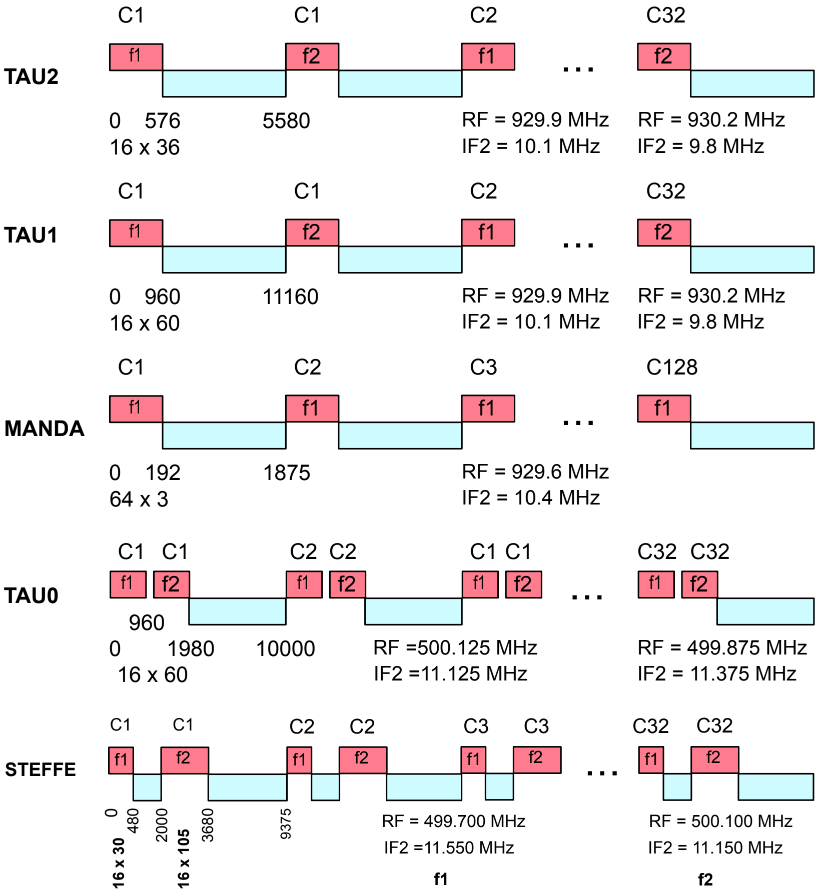

Figure 17: Transmission timing diagrams of some common EISCAT experiments.The schemes TAU1, TAU2 and MANDA are for the Tromsø UHF radar, while TAU0 and STEFFE are for the EISCAT Svalbard radar. The diagrams are not drawn to scale, but the labels indicate the length of the transmission (e.g., 576 μs in TAU2), the length of the interpulse period (5580 μs), and the transmission frequencies, both the RF frequency and the second IF frequency which is sampled by the SD receiver. All the transmissions are binary phase-coded. The number of code "bits" and their duration is also shown (16 bits × 36 μs). The bit patterns are from a set of N codes, where $N = 2\times$ number of bits. The code order in a given frequency channel is $C_1 \ldots C_N$ in TAU2–MANDA and STEFFE, but (for clutter cancellation purpose) C_1, C_2, C_1, C_2, C_3, C_4, $C_3 \ldots C_{32}$ in TAU0. Therefore, in TAU0, ranges from 3000 km up are ambiguous, while in the other experiments the first ambiguous range is much further away. Though not indicated in the diagram, the transmission blocks are surrounded by a receiver protection window, typically starting about 50 μs in front, and extending at least 100 μs after, the transmission. During the protection window, the receiver is closed to the sky but takes in a sample of the transmission waveform.

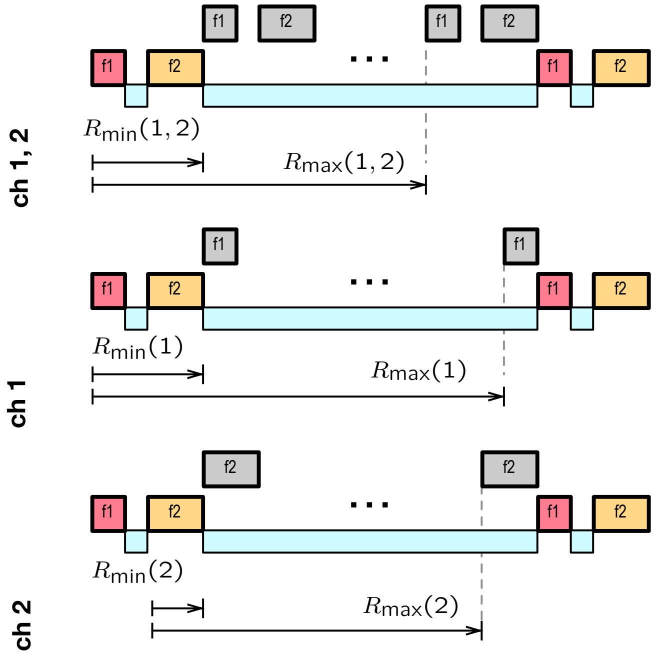

Figure 18: Optimizing range coverage in the STEFFE experiment in the match function method. Only matching in the second reception window is shown. We do not use the very first, low altitude window. We do use the third window, the one after the second short pulse, and the fourth window (not shown), after the second long pulse, so the actual maximum ranges are much larger than is marked in these diagrams. When one can only use only one of the pulses, the shorter pulse (f_1) gives the better range coverage. This report refers by “STEFFES” to STEFFE data analysed using only the shorter pulse. In effect, we make use only of the frequency channel 1 data; but note that for our point-like targets, the channel separation is achieved by the gating in time. Though it helps that the frequencies f_1 and f_2 are separated, for that reduces clutter due to any residual match of pulse 1 against the echo of pulse 2. The match would be small even if the frequencies were the same because of the phase-coding, but it is even smaller when also the frequencies are different.

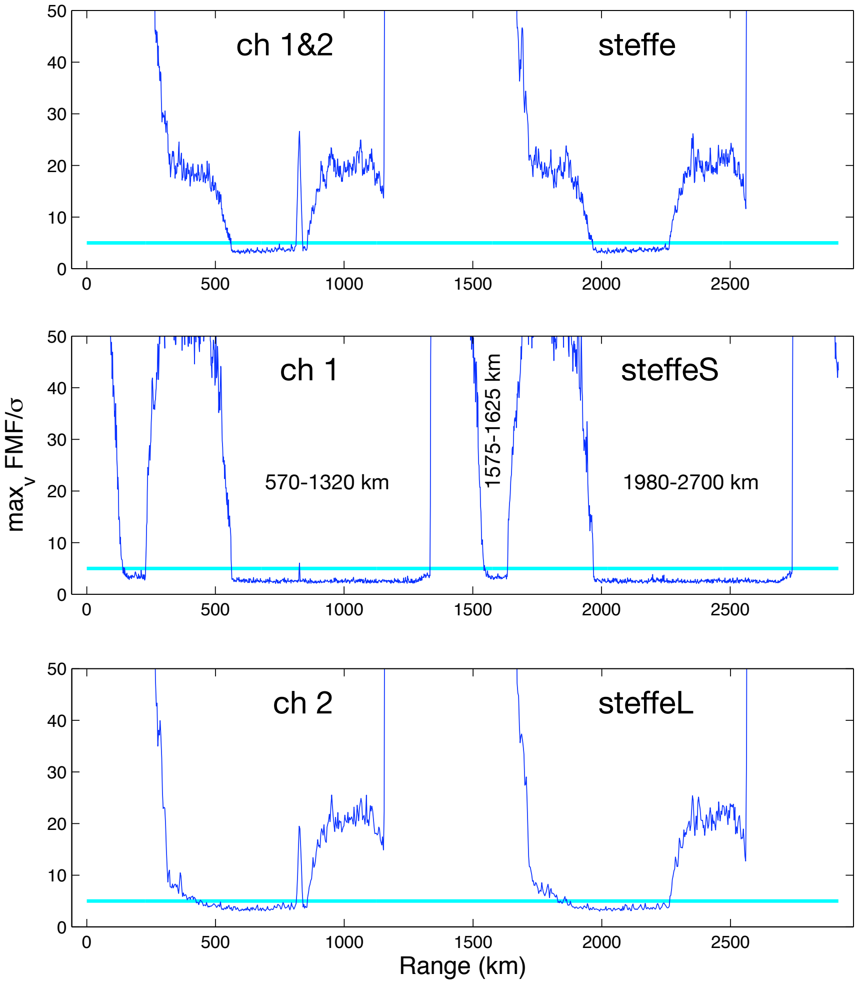

Figure 19: Actual range coverage in the STEFFE experiment in the MF-method. The top panel shows the result of matching with both transmitted pulses. The middle panel the result when matching with only the shorter pulse (the indicated intervals where those actually used for the data shown in this report). The bottom panel shows the result of matching with only the longer transmitted pulse. There is an actual target echo at about 800 km range, the huge bumps result when matching transmission against transmission. These data were taken with 1000 MHz sampling, with the IF2 center frequency of 11.000 MHz. This arrangement causes the signal echo from the shorter pulse, at 11.550 MHz, to be relatively more suppressed in the decimation filtering than the longer pulse, which is at 11.150 MHz. The signal peak height is proportional to the square root of the total signal energy, so, inherently, the longer pulse should give a peak that is only about twice as high ($\sqrt{1680/480}$). It is also clear from the bottom panel that using the longer pulse would necessitate range-dependent detection threshold thoughout most of the available range.

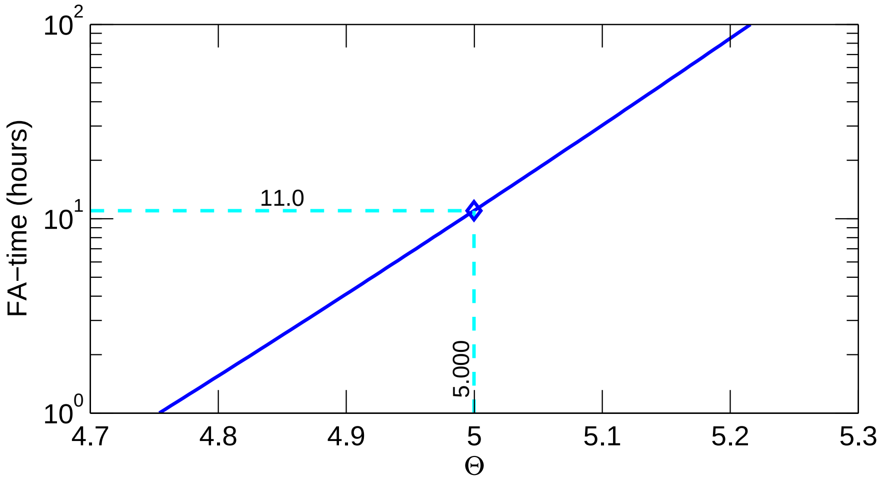

Figure 20: False alarm time v detection threshold in STEFFES in coherent integration. The plot is based on Eq. (2.27) in [3], with 1000 range gates and maximum monitored velocity 5 $\mathrm{km\,s^{-1}}$. The actual number of range gates searched in detection was 1018, but these would not all be statistically independent, and the false alarm time, 11 hours for the detection threshold 5.0, is probably a slight underestimate.

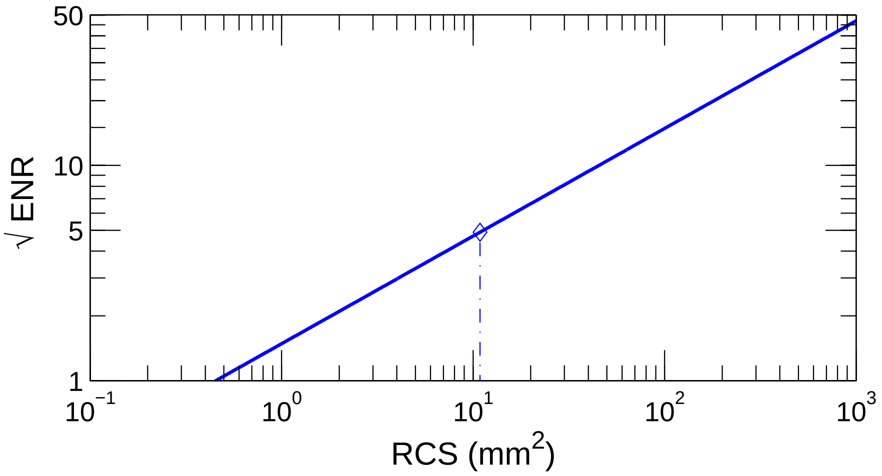

Figure 21: Expected energy-to-noise ratio as function of RCS in STEFFES. The ESR 42 m antenna with gain 45.3 dBi, range 1000 km, system temperature 70 K and 0.2 s coherent integration are assumed. RCS 10.9 mm^2 corresponds to the detection threshold, ENR = 24. The corresponding effective diameter is 3.56 cm.

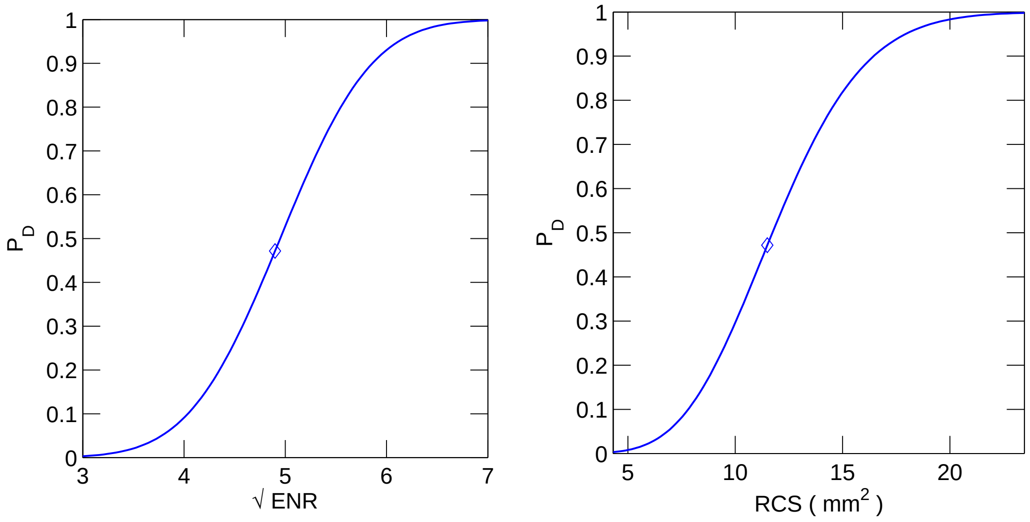

(a) (b)

Figure 22: Probability of detection in STEFFES when using coherent integration. The standard detection threshold $\max \mathrm{MF}/\sigma = 5$ is assumed. Panel (a) shows probability of detection as a function of the signal energy-to-noise ratio ENR, this relation does not depend on experiment parameters. Panel (b) plots the same curve, but now as a function of radar cross section for the case of STEFFES with 1000 km range and 0.2 s coherent integration. In both panels, the marker corresponds to signal energy that is just at the nominal detection threshold, $\mathrm{ENR} = 24$ and $\mathrm{RCS} = 10.9\ \mathrm{mm}^2$, for which $P_\mathrm{D} = 0.47$. The curves are computed from Eq. (2.49) of [3].

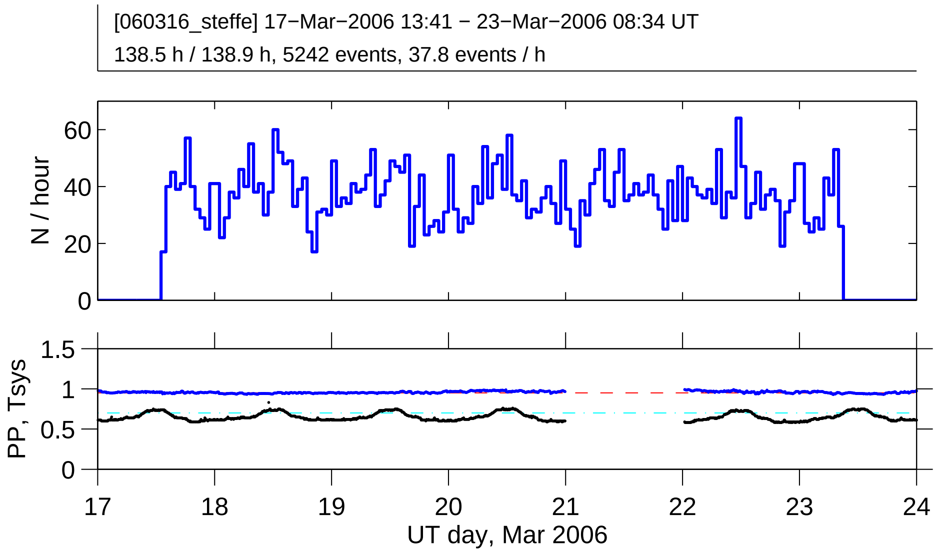

Figure 23: Summary of STEFFE campaign at ESR, March 2006. The header panel gives the start and stop times of the debris measurement, the total length of “valid” data collection (found by adding up all half-hour intervals between the campaign start and end times during which the final analysis found at least one event), the number of analysed events, and the mean number of analysed events per the actual data collection time. The middle panel gives the hourly number of debris events. The blue line in the bottom panel gives the transmission peak power in MW, taken from normal EISCAT data analysis results, the black curve gives the system temperature T_{sys}, in units of 100 K. In debris analysis, a constant value of 0.95 MW (red dashed line) was used for the transmission, and a constant value 70 K for the system temperature (green dashed line). The apparent gap in the the system parameter data is because there is a gap in (the access to) analysis results on March 21.

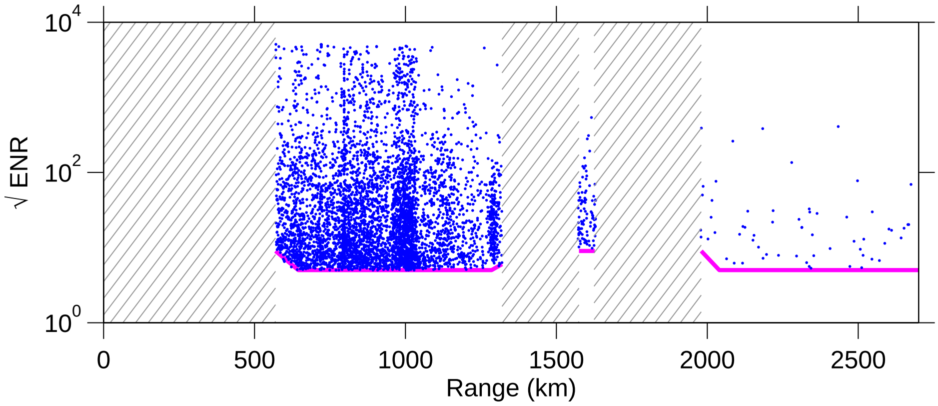

Figure 24: STEFFES at ESR, March 2006, signal energy versus time, all events. The y-axis is the maximum value of the match function divided by noise standard deviation. Apart from including a background bias, this is equal to the square root of the signal energy-to-noise ratio $\mathrm{ENR} = E_\mathrm{s}/kT_\mathrm{sys}$, so that the y-axis, more precisely, could be labeled with $\sqrt{\mathrm{ENR}+1}$. The detection threshold is a line with vertexes at (x, y)-points (570,9), (640,5), (1286,5), (1320,6), (1575,9), (1628,9), (1980,9), (2040,5) and (2700,5). The downward ramps between ranges 570 and 640 km and the aliased interval from 1980 km to 2040 km are to counter clutter due to the topside ionosphere. For thermal noise, and fully efficient coherent integration, the threshold level 5 corresponds to false alarm time somewhat in excess of 10 hours. The constancy over range of the maximum observed ENR suggests that the strongest signals have been clipped by the receiver (either the EISCAT receiver, or the space debris receiver).

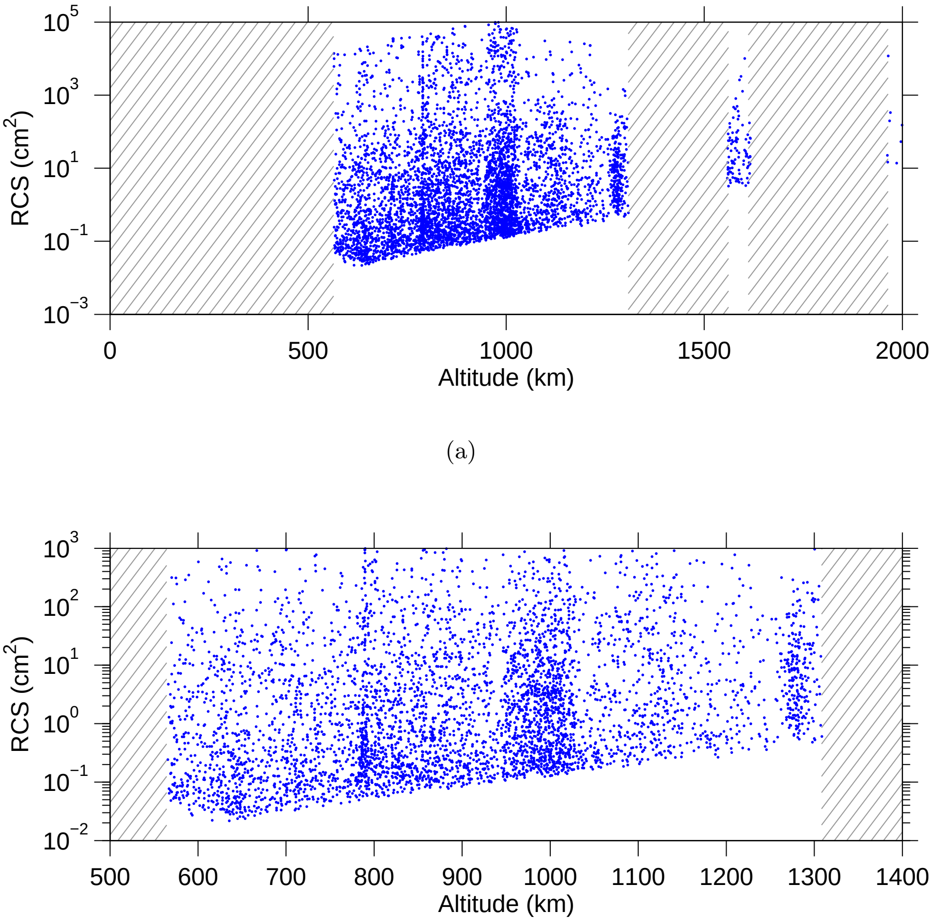

(a)

(b)

Figure 25: STEFFES at ESR, March 2006, cross section versus altitude.

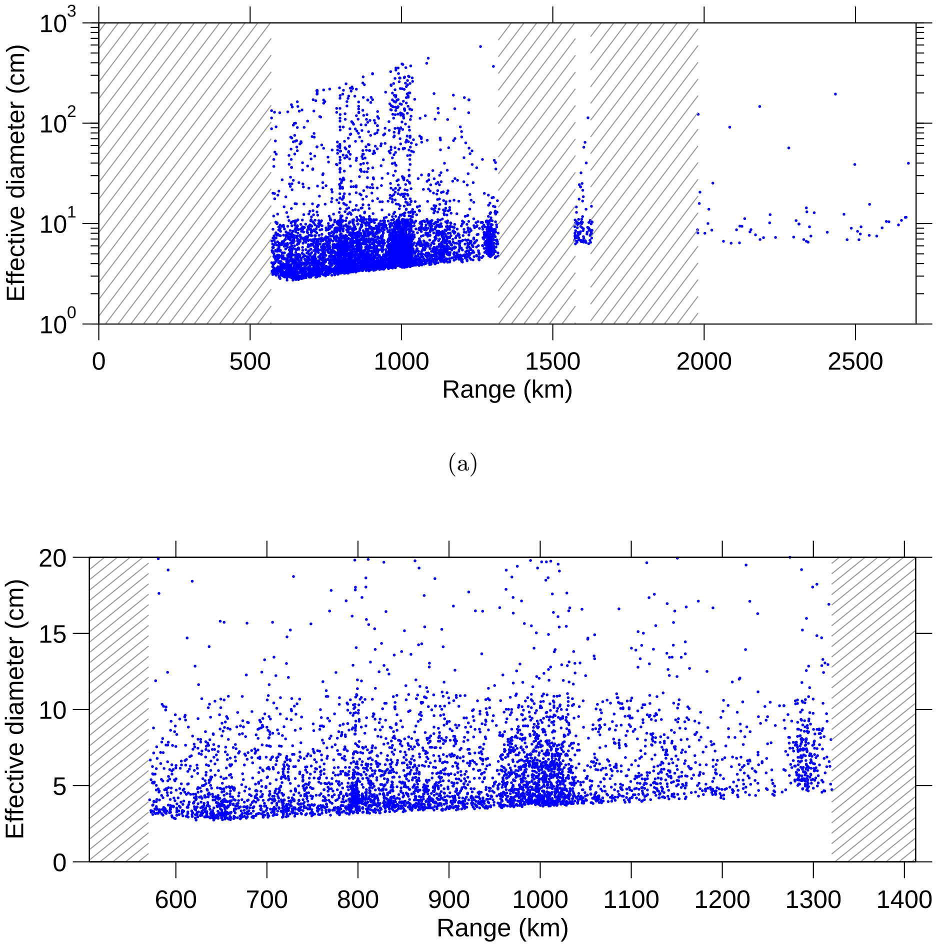

(a)

(b)

Figure 26: STEFFES at ESR, March 2006, effective diameter versus range.

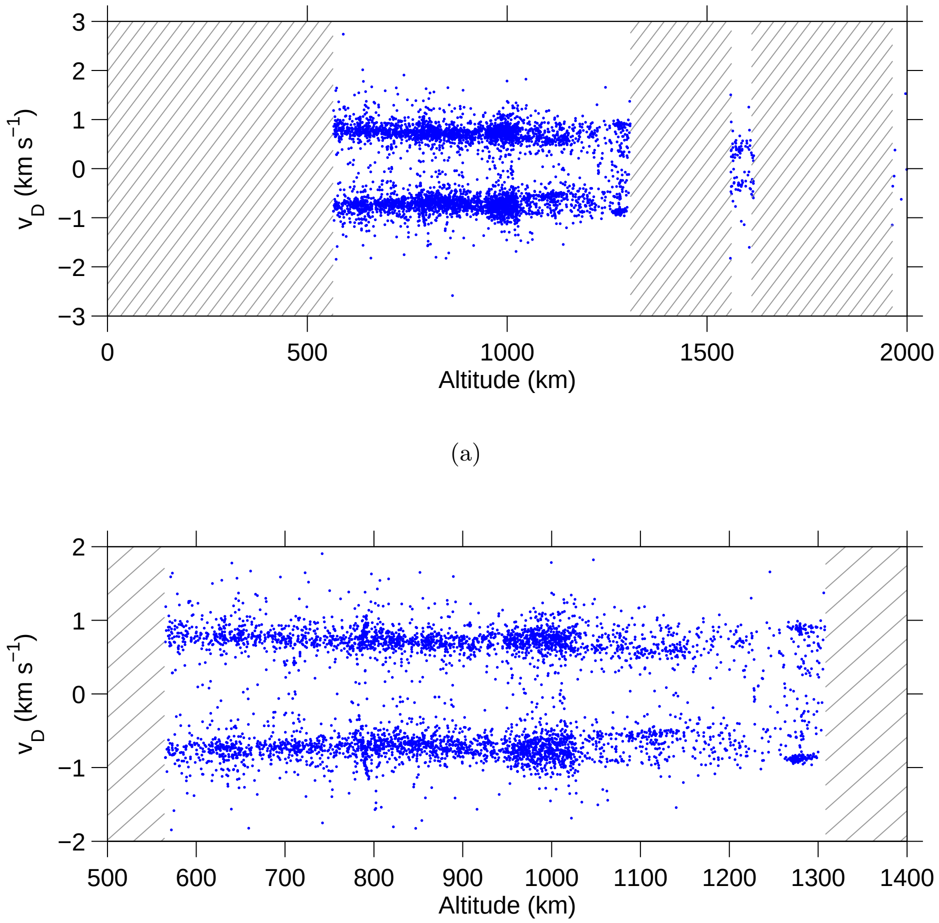

(a)

(b)

Figure 27: STEFFES at ESR, March 2006, radial velocity versus altitude.

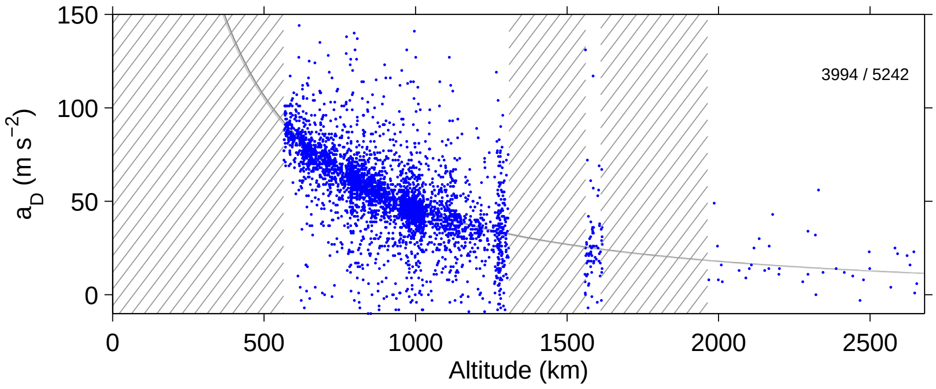

(a)

Figure 28: STEFFES at ESR, March 2006, radial acceleration versus altitude.

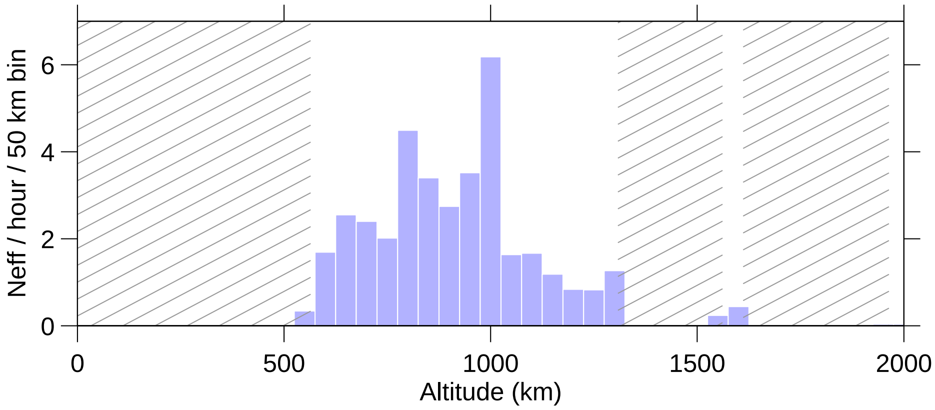

(a)

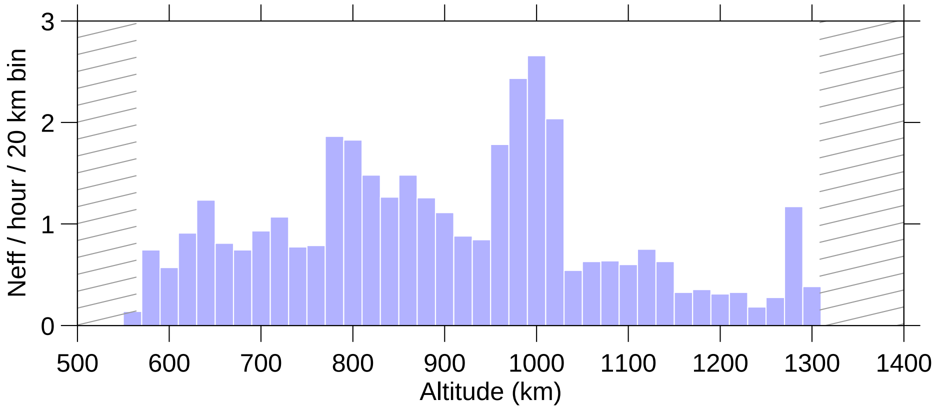

(b)

Figure 29: STEFFES at ESR, March 2006, event rate as function of altitude.

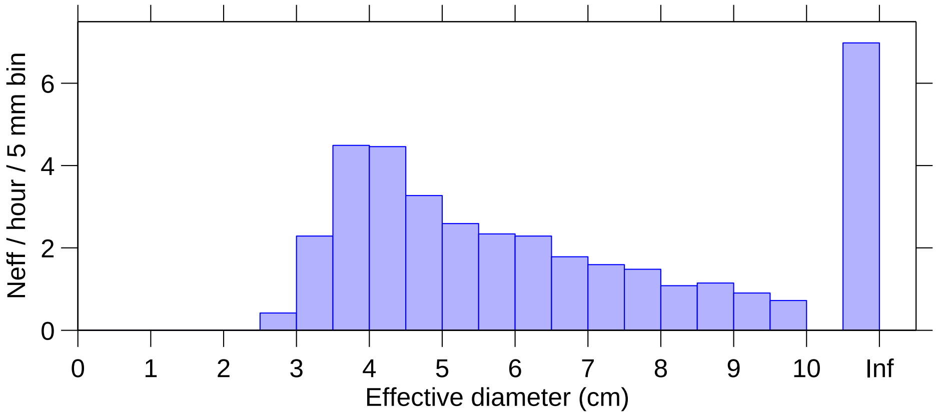

(a)

Figure 30: STEFFES at ESR, March 2006, event rate as function of effective diameter.

Figure 31: STEFFELEO: ESR antennas, in the early hours of July 9, 2006. The 32 antenna (left) is pointed towards East, azimuth 90°, at 75°elevation. The magnetic-field-aligned ESR 42 m antenna (right) was not used in the beam park measurement.

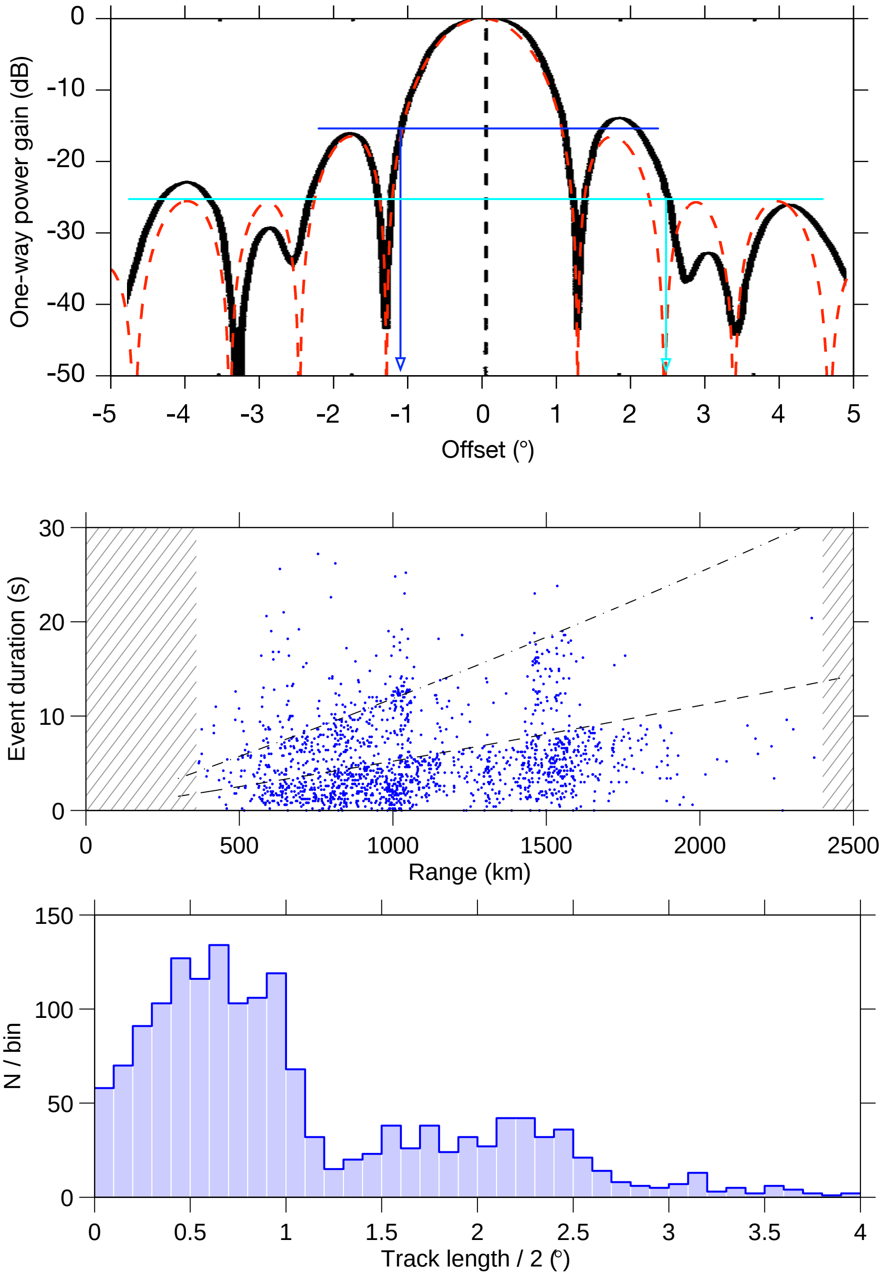

Figure 32: STEFFELEO: ESR 32 m antenna's gain pattern. In the top panel, the dashed red line is a simple theoretical gain model, the solid black line is the measured power gain of EISCAT Tromsø 32m antenna, scaled by wavelength difference. The 3 dB beam width is 2 × 0.55°, and the maximum gain is 42.5 dBi. The middle and bottom panels show how the antenna pattern manifests itself in the beam crossing time. The middle panel shows the duration of objects' visibility versus range. The bottom panel shows the number of objects as a function of the angular size of the arc of visibility, computed from the measured duration of visibility and an assumed circular-orbit angular velocity.

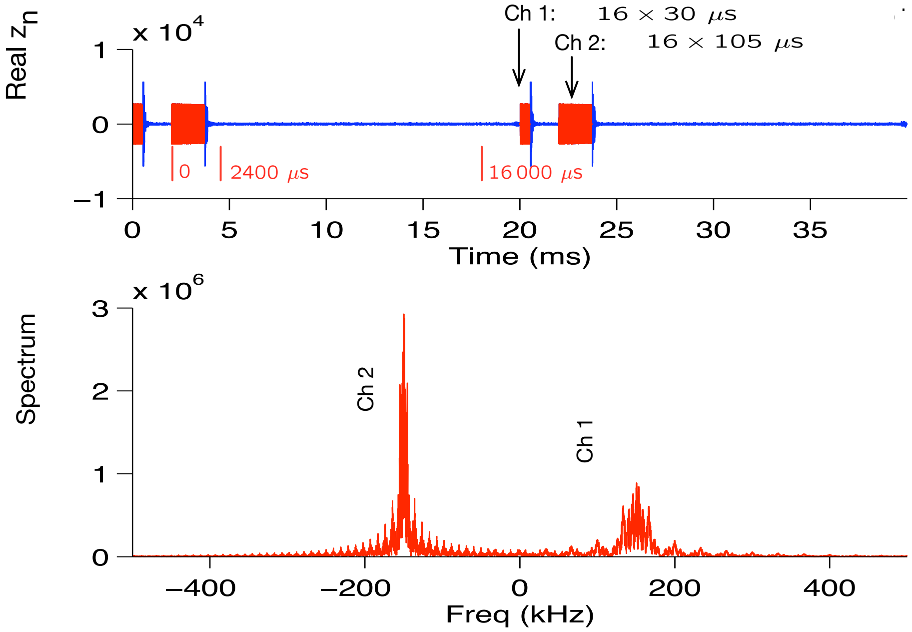

Figure 33: STEFFELEO: Two 20 ms IPPs of raw data. Top panel shows real part of the complex samples, bottom panel shows the magnitude of the spectrum computed from the transmission samples, which are shown in red in the top panel. The sample interval in storage is 1 μs. With four bytes per complex point, the data accumulation rate to disk is 14.4×10^9 bytes/hour. The shorter of the two transmissions, "ch1", a 16 × 30 μs binary phase code from the alternating code family of modulation patterns, was *not* used in the debris data processing. The 1680 μs long pulse, "ch2", is also a 16 bit alternating code, with baud length of 105 us. In our ambiguity-function based data processing—the "match function" method—the ch2 transmitted pulse is cross-correlated with the reception, starting 2400 μs after the start of the pulse, and finishing 16 000 μs after the pulse start. This gives range coverage from 360 km to 2400 km and altitude coverage from 349 km to 2341 km.

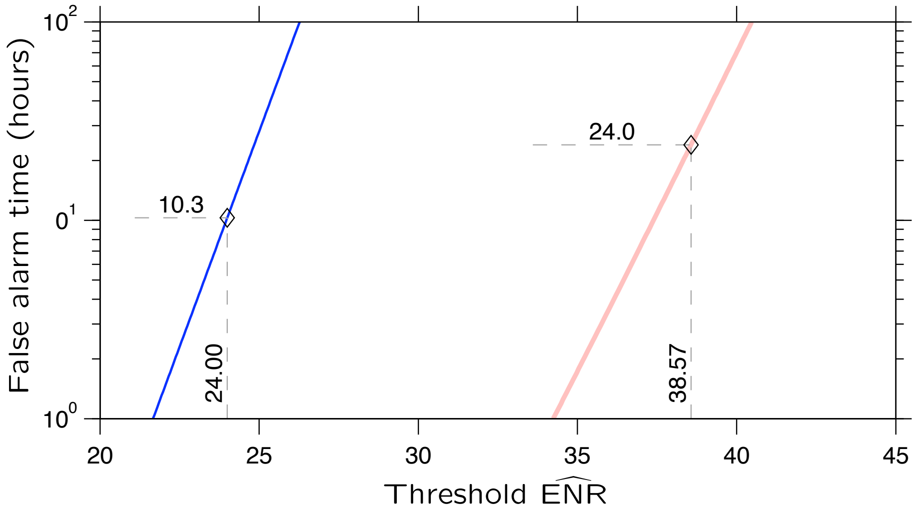

Figure 34: STEFFELEO: False alarm time as function of detection threshold. The left line is for 0.3 s coherent integration, the right line is for 0.3 s non-coherent integration. The threshold is expressed in terms of the estimated energy-to-noise ratio $\widehat{\text{ENR}}$. In coherent integration, for most part of the target range, we used threshold $\widehat{\text{ENR}} = 24$ which corresponds to false alarm time of 10 hours. In non-coherent integration, we used threshold 39 which corresponds to false alarm time of 24 hours.

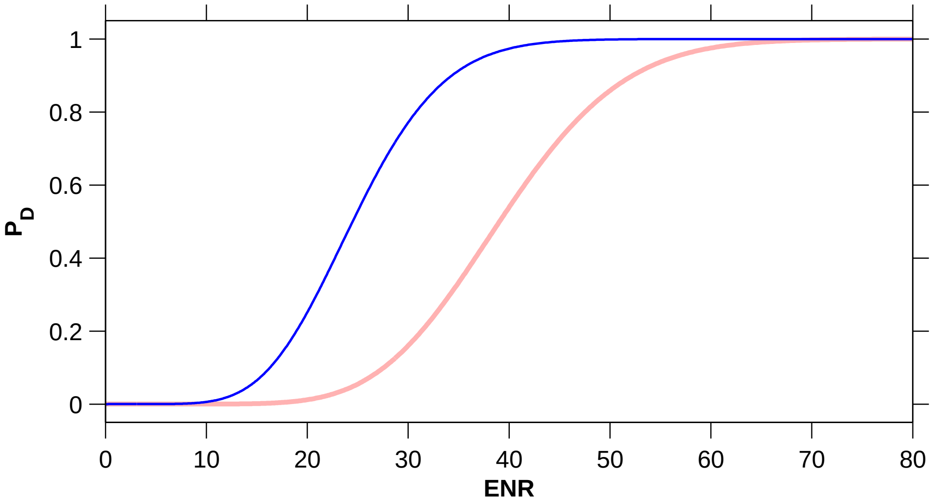

Figure 35: STEFFELEO: Probability of detection as function of (actual) ENR. The left-hand curve is for 0.3 s coherent integration with threshold 24, the right-hand curve for 0.3 s non-coherent integration with threshold 39.

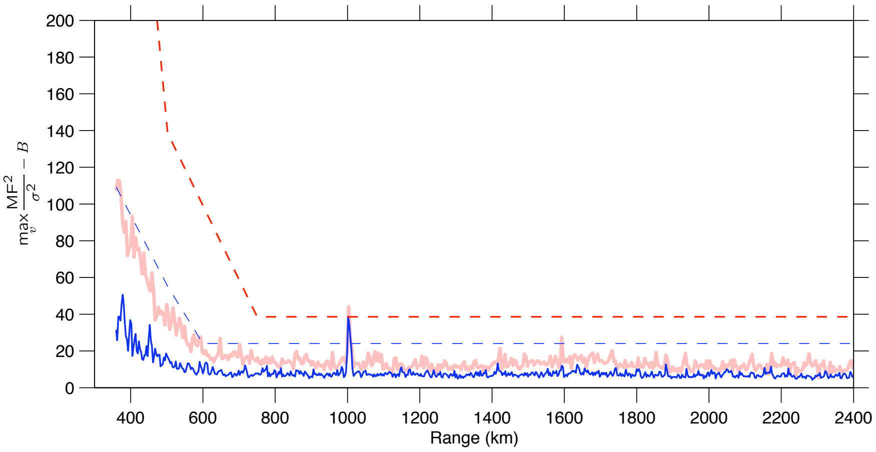

Figure 36: STEFFELEO: Detection. Detection is based on the estimated energy-to-noise ration, the maximum value of the ENR (the peak at about 1000 km range in this figure) exceeding a threshold. This figure shows a detection both with coherent integration (blue color) and non-coherent integration (red color). The solid line is the velocity-maximised, background subtracted match function $y(R) = \max_v \mathrm{MF}(v, R)/\sigma^2 - B$. In coherent integration, the background $B = 1$, in non-coherent integration, $B = 15$. The dashed line is the range-dependent threshold.

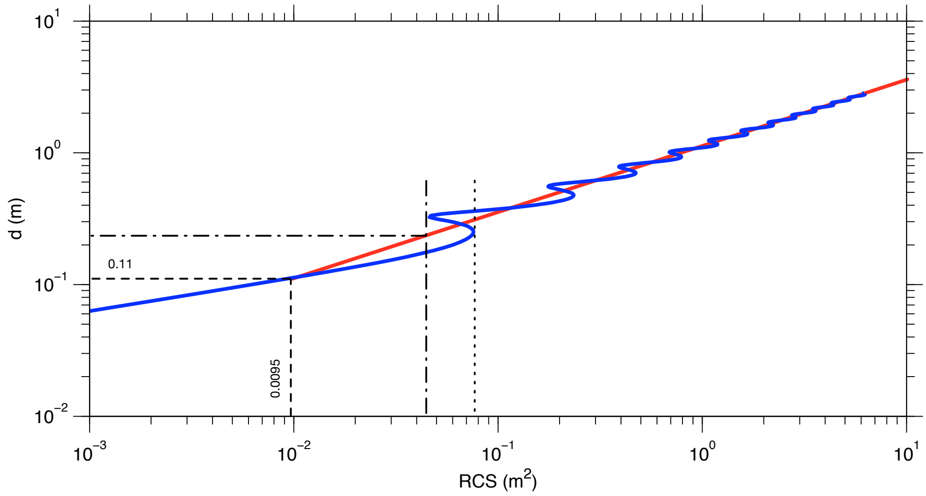

Figure 37: STEFFELEO: Converting RCS to diameter. We use a simplified model (red line) for the cross section of the conducting sphere, where we ignore the resonance region. This leads to considerable overestimation of target size near the small-size end of the resonance region.

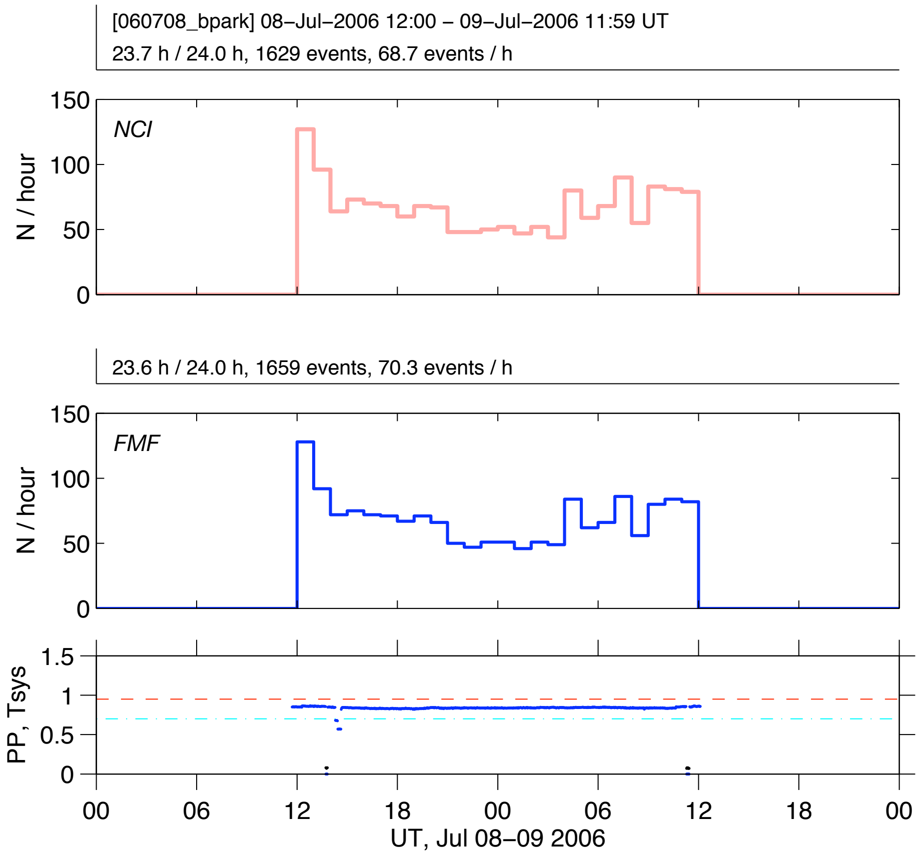

Figure 38: STEFFELEO: Hourly number of objects. The top panel is for non-coherent integration, the middle panel for FMF-based coherent integration. The bottom panel indicates transmission peak power in MW and system noise temperature in 100 K. For RCS estimates, the constant peak power of 0.95 MW and constant system temperature 70 K were used. Lamentably, there is considerable uncertainty about the actual peak power, for different monitoring systems gave inconsistent results during the measurement. It is possible that the power was between 10–and 15% lower than was assumed in the analysis. The transmission was quite stable, though, and there were only two breaks, each a few minutes long.

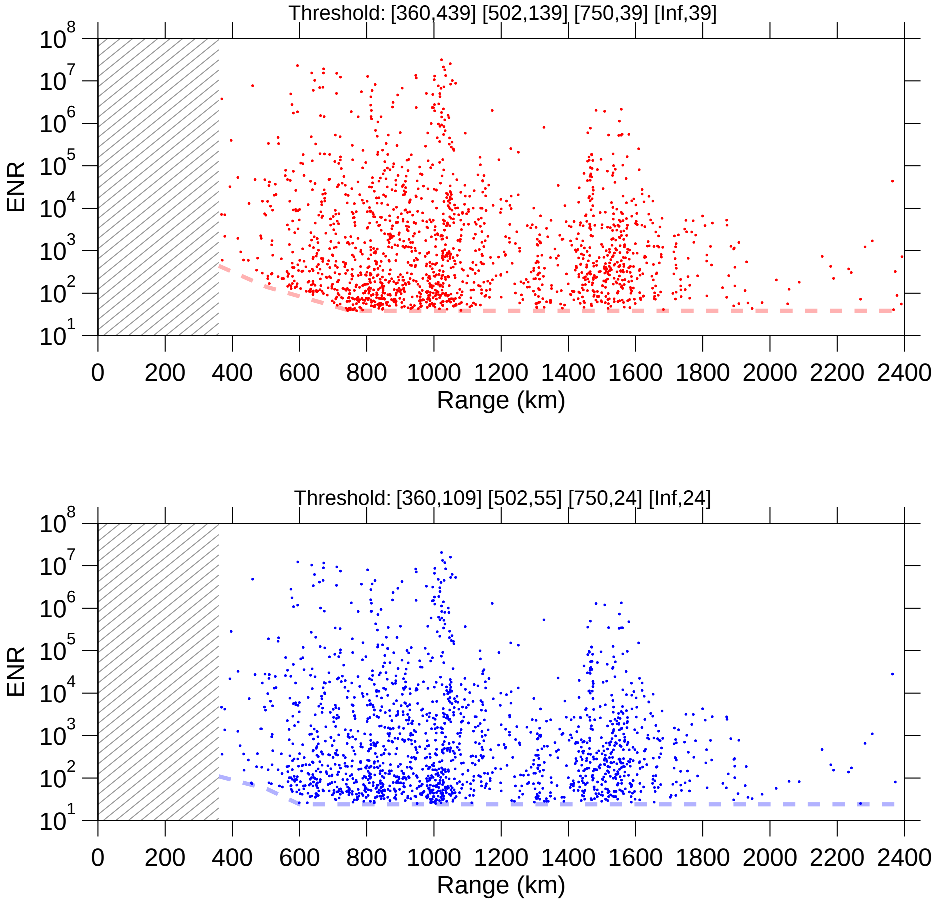

Figure 39: STEFFELEO: ENR against range, 0.3 s integration. Top panel is for non-coherent integration, bottom panel for coherent integration. The dashed lines show the detection threshold, the vertices of the lines are listed in the panel headers. The detection in both integration scheme was done with 0.3 s integration time, but the parameter analysis for coherent integration was done with 0.2 s integration time. The resulting ENR estimates for the coherent integration have been scaled by 3/2 to refer them back to the 0.3 s integration time for plotting (ENR in the result files for CI refer to 0.2 s integration). In the non-coherent integration, also the parameter estimation used 0.3 s integration time.

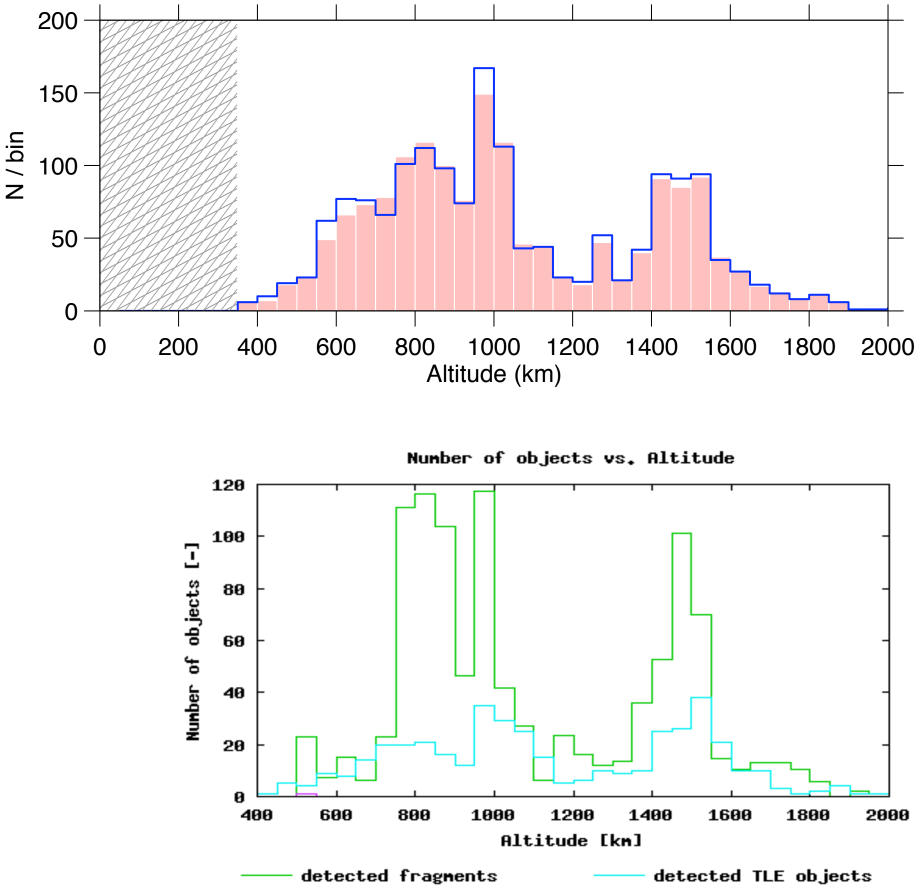

Figure 40: STEFFELEO: Number of events v altitude.The top panel is the EISCAT measurement. The red bars are for non-coherent integration, the blue line for coherent integration. The bottom panel shows our preliminary effort to handle the measurement with ESA's PROOF^{2005} tool.

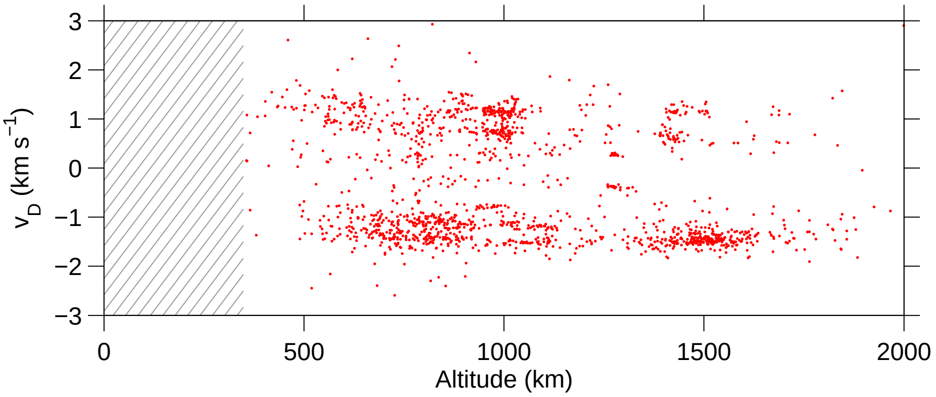

(a) Range rate versus altitude in non-coherent integration.

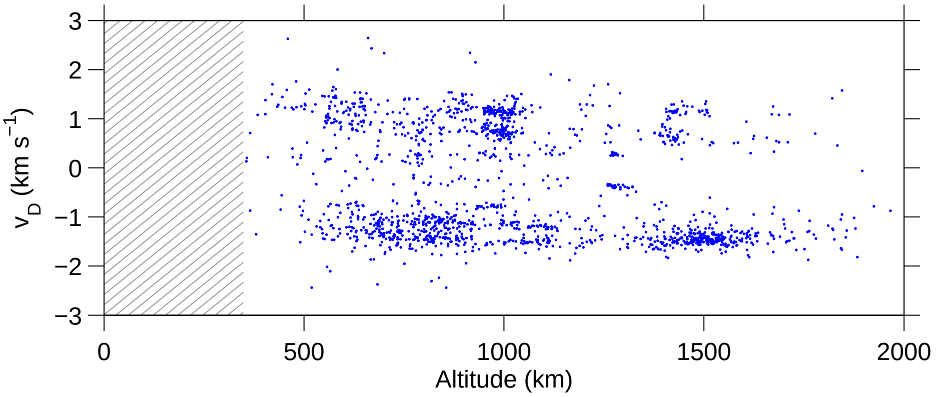

(b) Range rate versus altitude in FMF coherent integration.

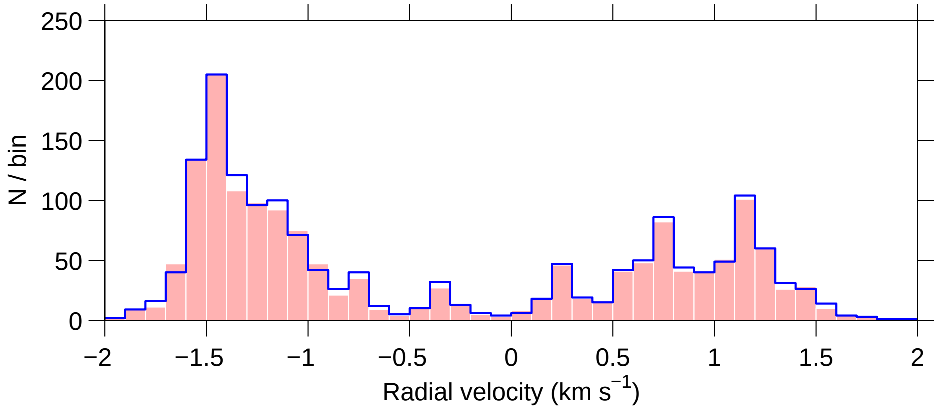

(c) Number of objects v range rate in NCI (red bars) and FMF (blue line).

Figure 41: STEFFELEO: Doppler-velocity data.

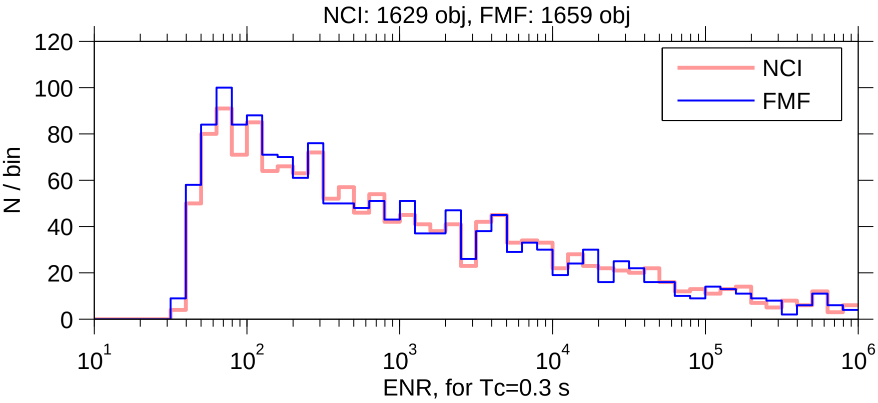

(a) Event count per bin as function of ENR, integrated over all ranges.

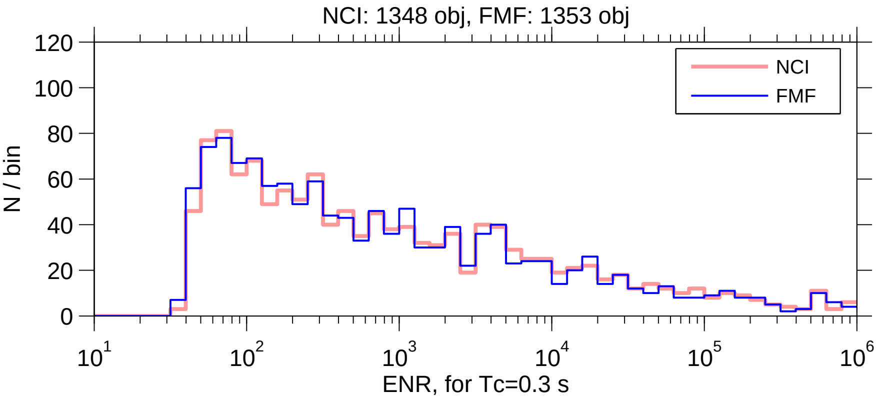

(b) Event count per bin, integrated over ranges > 750 km.

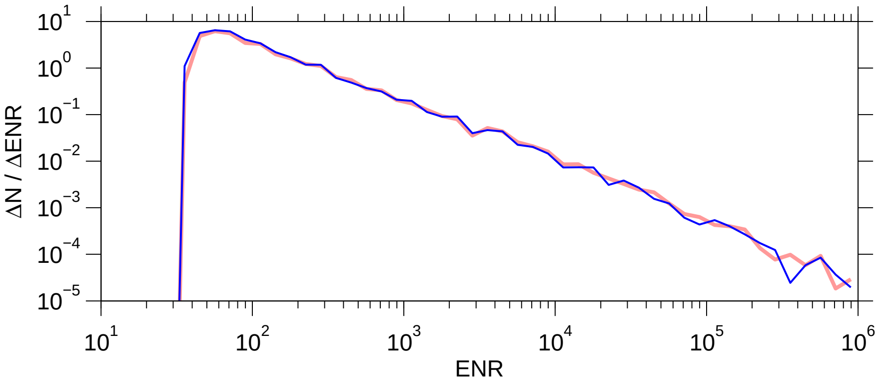

(c) Event count per bin divided by bin width, as function of ENR.

Figure 42: STEFFELEO: ENR distribution. The histograms are based on Fig. 39, integrating in the range direction.

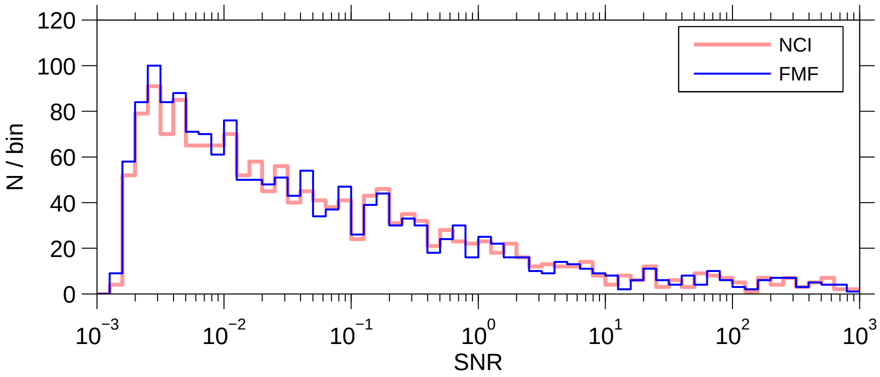

(a) Event count per bin as function of SNR, integrated over all ranges.

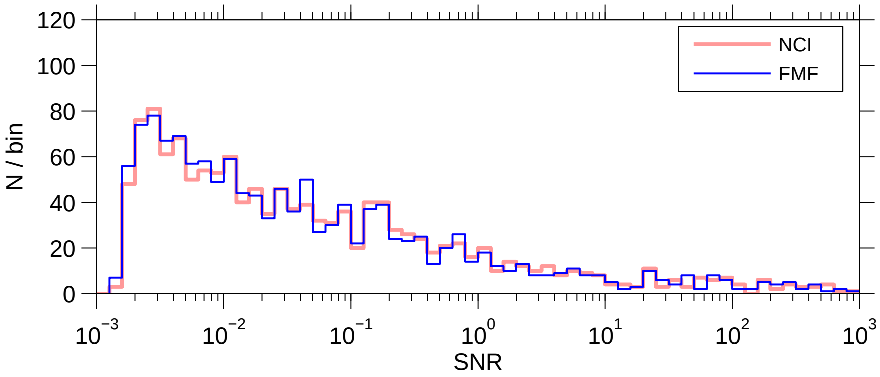

(b) Event count per bin, integrated over ranges > 750 km.

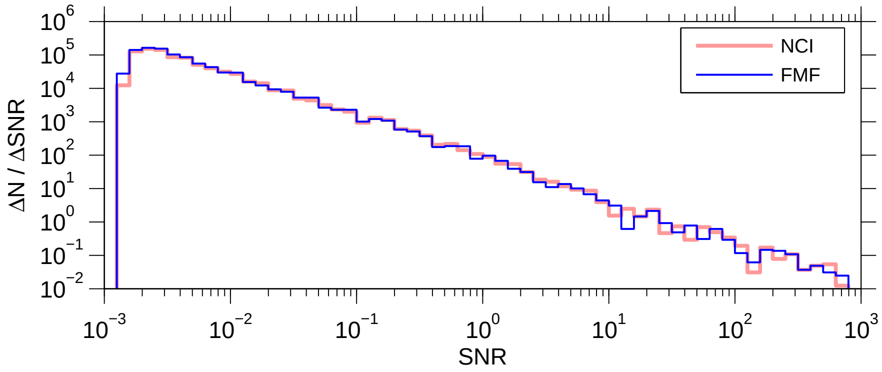

(c) Event count per bin divided by bin width, as function of SNR.

Figure 43: STEFFELEO: SNR distribution. The histograms are based on Fig. 39, integrating in the range direction.

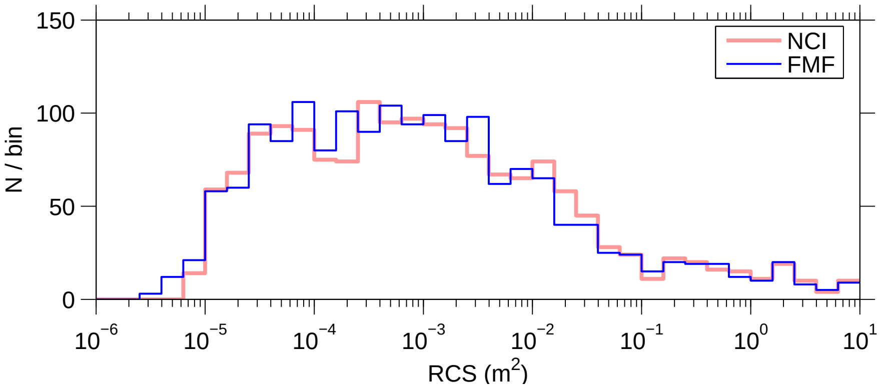

(a) Event count per bin as function of $\mathrm{RCS}_{\mathrm{min}}$, integrated over all ranges.

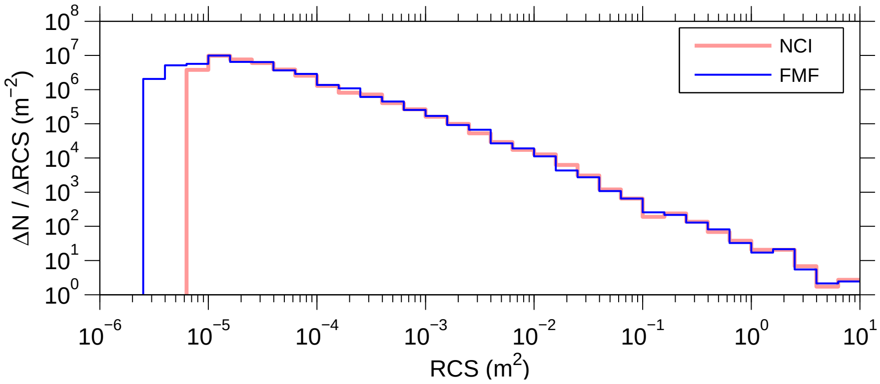

(b) Event count per bin divided by bin width, as function of $\mathrm{RCS}_{\mathrm{min}}$.

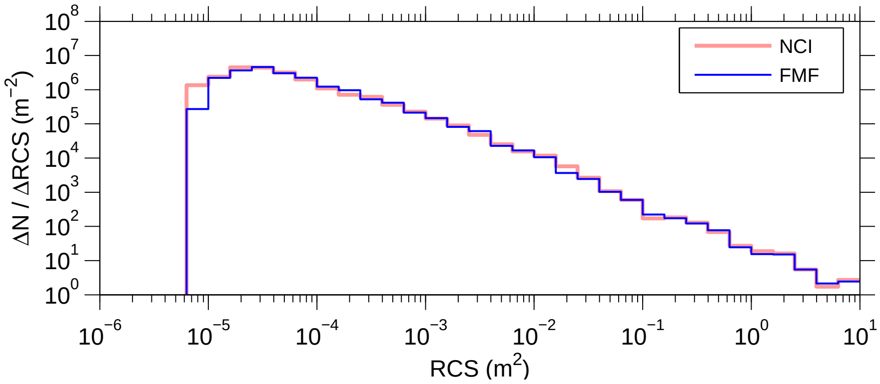

(c) Event count per bin, integrated over ranges > 750 km.

Figure 44: STEFFELEO: $\mathrm{RCS}_{\mathrm{min}}$ distribution. These histograms are based on Fig. 39, integrating in the range direction.

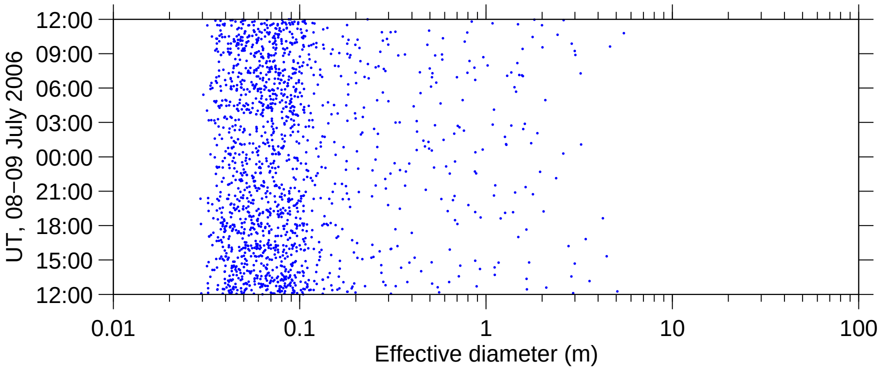

(a) Objects' observation instant versus effective diameter.

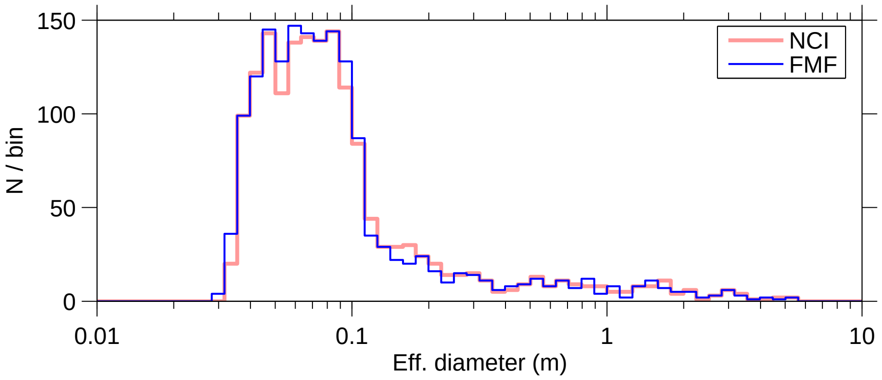

(b) Event count per bin as function of d_{eff}, integrated over all ranges.

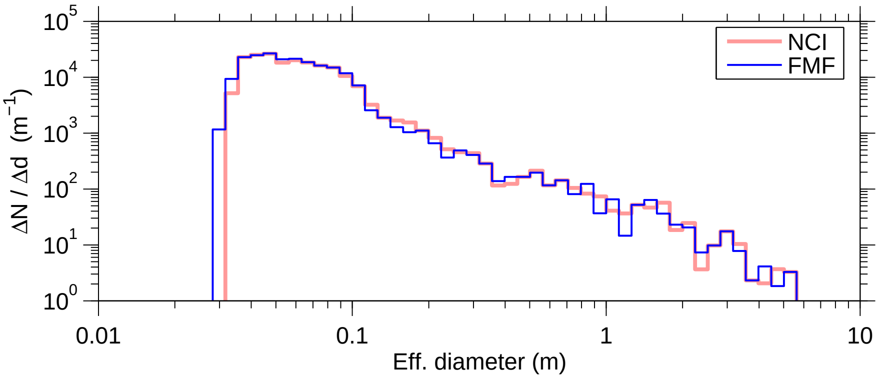

(c) Event count per bin divided by bin width, as function of d_{eff}.

Figure 45: STEFFELEO: Distribution of objects' effective diameter. The histograms are based on Fig. 39, integrating in the range direction.